**DOT/FAA/TC-26/7**

Federal Aviation Administration
William J. Hughes Technical Center
Aviation Research Division
Atlantic City International Airport
New Jersey 08405

# Measurement and Modeling of Hazardous Substances Produced in Fires Fueled by Polymeric Materials

March 2026

Final report

U.S. Department of Transportation
**Federal Aviation Administration**

## NOTICE

This document is disseminated under the sponsorship of the U.S. Department of Transportation in the interest of information exchange. The U.S. Government assumes no liability for the contents or use thereof. The U.S. Government does not endorse products or manufacturers. Trade or manufacturers' names appear herein solely because they are considered essential to the objective of this report. The findings and conclusions in this report are those of the author(s) and do not necessarily represent the views of the funding agency. This document does not constitute FAA policy. Consult the FAA sponsoring organization listed on the Technical Documentation page as to its use.

This report is available at the Federal Aviation Administration William J. Hughes Technical Center's Full-Text Technical Reports page: actlibrary.tc.faa.gov in Adobe Acrobat portable document format (PDF).

Technical Report Documentation Page

**Form DOT F 1700.7** (8-72) Reproduction of completed page authorized

| 1. Report No. | 2. Government Accession No. | 3. Recipient's Catalog No. |
|---|---|---|
| DOT/FAA/TC-26/7 | | |

| 4. Title and Subtitle | 5. Report Date |
|---|---|
| Measurement and Modeling of Hazardous Substances Produced in Fires Fueled by Polymeric Materials | March 2026 |
| | 6. Performing Organization Code |

| 7. Author(s) | 8. Performing Organization Report No. |
|---|---|
| Farnaz Beygi Khosroshahi and Stanislav I. Stoliarov | |

| 9. Performing Organization Name and Address | 10. Work Unit No. (TRAIS) |
|---|---|
| University of Maryland, Department of Fire Protection Engineering, College Park, MD 20742 | 11. Contract or Grant No. |

| 12. Sponsoring Agency Name and Address | 13. Type of Report and Period Covered |
|---|---|
| Federal Aviation Administration | 14. Sponsoring Agency Code |

15. Supplementary Notes

16. Abstract

A new methodology was developed to conduct combustion experiments under constant global equivalence ratio (*GER*) conditions using a modified Fire Propagation Apparatus (FPA). The approach maintains fixed ventilation by applying calibrated, time-dependent air-flow profiles, enabling *GER* to remain constant despite continuous changes in fuel-pyrolysis rate. This method overcomes a key limitation of conventional FPA testing, in which time-varying *GER* introduces uncertainty in relating species yields and heat release to ventilation conditions. Continuous measurements of $O_2$, $CO_2$, CO, total hydrocarbons, particulate matter, NO, and HCN were obtained using calibrated analyzers, and the characteristic residence time of the combusting mixture in the test section was incorporated into the analysis framework.

The capabilities of the method were demonstrated through a series of constant-*GER* tests on poly(methyl methacrylate) (PMMA) over a wide range of ventilation conditions. Increasing *GER* produced monotonic decreases in $CO_2$ yield and effective heat of combustion and corresponding increases in CO, particulate matter, and hydrocarbon yields. Species production also showed systematic dependence on the characteristic residence time of the reacting mixture, indicating that both *GER* and residence time govern combustion efficiency and effluent composition. An empirical model was developed to predict species yields and effective heat of combustion as functions of these controlling parameters.

The methodology was further applied to oriented strand board (OSB) to assess its suitability for materials exhibiting charring behavior and more complex pyrolysis. Constant-*GER* conditions were successfully implemented, and species yields and effective heat of combustion displayed strong dependence on both *GER* and residence time, demonstrating the method's applicability to a broader class of fuels.

| 17. Key Words | 18. Distribution Statement |
|---|---|
| Fire Propagation Apparatus, new diagnostics, under-ventilated fires, fire effluent composition, toxicity, CO, soot, total hydrocarbons | This document is available to the U.S. public through the National Technical Information Service (NTIS), Springfield, Virginia 22161. This document is also available from the Federal Aviation Administration William J. Hughes Technical Center at actlibrary.tc.faa.gov. |

| 19. Security Classif. (of this report) | 20. Security Classif. (of this page) | 21. No. of Pages | 22. Price |
|---|---|---|---|
| Unclassified | Unclassified | 75 | |

# Contents

## Figures

## Tables

## Acronyms

| Acronym | Definition |
|---|---|
| FID | Flame Ionization Detector |
| FPA | Fire Propagation Apparatus |
| *GER* | Global Equivalence Ratio |
| HRRPUA | Heat Release Rate per Unit Area |
| LPM | Liters per minute |
| MFC | Mass-Flow-Controller |
| MLR | Mass Loss Rate |
| NDIR | Non-Dispersive Infrared |
| OSB | Oriented Strand Board |
| PM | Particulate Matter |
| PMMA | Poly(methyl Methacrylate) |
| THC | Total Hydrocarbons |

# 1 Introduction

To fully characterize fire hazards associated with an aircraft fire, it is important to quantify not only the rate of generation of heat and its evolution in time but also the rate of generation of hazardous combustion products. Unfortunately, at present, there is no standard laboratory-scale test method that can be used to determine the hazardous product generation by a given material over a wide range of fire conditions. The most well-established methods to characterize fire effluent include ISO TS 19700 apparatus (ISO-TS-19700, 2007) and the Fire Propagation Apparatus (FPA) (ASTM International, 2019). In both methods, the product yield information can be collected as a function of equivalence ratio, which is defined as:

$$\phi = \frac{\left(\frac{mass_{air}}{mass_{fuel}}\right)_{\text{stoichiometric}}}{\left(\frac{mass\ flow_{air}}{mass\ flow_{fuel}}\right)_{\text{actual}}}.$$

In the ISO TS 19700 apparatus, flaming combustion takes place in a small (5 cm diameter) tubular furnace purged with a laminar air flow. The test results strongly depend on the furnace temperature – the parameter that is not directly associated with any characteristics of full-scale fires. In FPA, the fire dynamics and size (5-15 kW) more closely resemble a realistic fire scenario. However, standard diagnostics used in this apparatus include only measurement of CO, $CO_2$ and optical density of smoke and, thus, provide rather limited information on fire effluent composition.

## 1.1 Objectives

The first objective of the current research project was to develop a bench-scale test method that accurately replicates the full range of fire conditions encountered in fully developed and post-flashover fires and enables accurate quantification of hazardous product yields. The second objective was to develop a more complete understanding of the combustion conditions that control the yields of hazardous products. The third objective was to develop empirical models that relate hazardous product yields from combustion of several representative polymeric materials to the key parameters that define relevant combustion conditions.

# 2 Method development

## 2.1 Fire Propagation Apparatus design and improvements

The FPA (in-house design) used in the current study was built in compliance with the ASTM standard (ASTM International, 2019) in terms of its dimensions and operational parameters. However, several modifications were made to improve manufacturability of its key components and accuracy and breadth of the measurements. As shown in Figure 1, the FPA consists of an aluminum air distribution chamber, quartz tubes, a sample holder, a load cell, four external high-temperature infrared (IR) heaters (only two are shown in the figure), a water-cooled shield, an ethylene-air premixed pilot flame burner, and an exhaust system containing multiple probes. A circular sample is positioned on the sample holder, which is located within the air distribution chamber. The side and bottom surface of the samples were wrapped with aluminum foil and thermally insulated with Kaowool PM™ ceramic fiber board.

The quartz tubes, with an inner diameter of 162 mm and total height of 765 mm, are mounted so that, during a test and with appropriate gas purge, the sample is isolated from the surrounding laboratory environment. The overall quartz tube height was increased by 106 mm from the standard height of 659 mm making it 765 mm to reduce potential air entrainment and thus, improve control of the atmosphere inside the test section. Using an Alicat ™ mass flow controller, air is introduced into the distribution chamber at a controllable flow rate up to 400 standard liters per minute (SLPM) (liters per minute at standard temperature and pressure of 25°C and 101,325 Pa, respectively) to supply ventilation to the test section. Constant air flow of 200 SLPM is used for standard testing (ASTM International, 2019). A 30-mm-thick layer of 3-mm-diameter glass beads, located below the sample holder, is used to homogenize the flow. The sample mass is measured during the experiment using a Sartorius load cell with a resolution of 0.01 g (a resolution of 0.1 g is specified in the standard). The raw mass signal is recorded at a frequency of 5 Hz.

A redesigned stainless steel water-cooled shield (an aluminum water-cooled shield is specified in the standard) is positioned between the IR heaters and the quartz tubes, preventing the sample from being exposed to radiant heat during the warm-up period of the heating lamps. After a two-minute warm-up period, the shield is lowered, exposing the sample to a calibrated radiant heat flux provided by the high-temperature IR heaters, which can deliver up to 110 kW $m^{-2}$ incident heat flux to the top surface of the sample. The radiant heat flux was calibrated by placing a reference heat flux gauge at the sample location and measuring the incident heat flux at different

lamp power levels. A calibration curve was then established to relate the lamp power setting to the heat flux imposed on the sample.

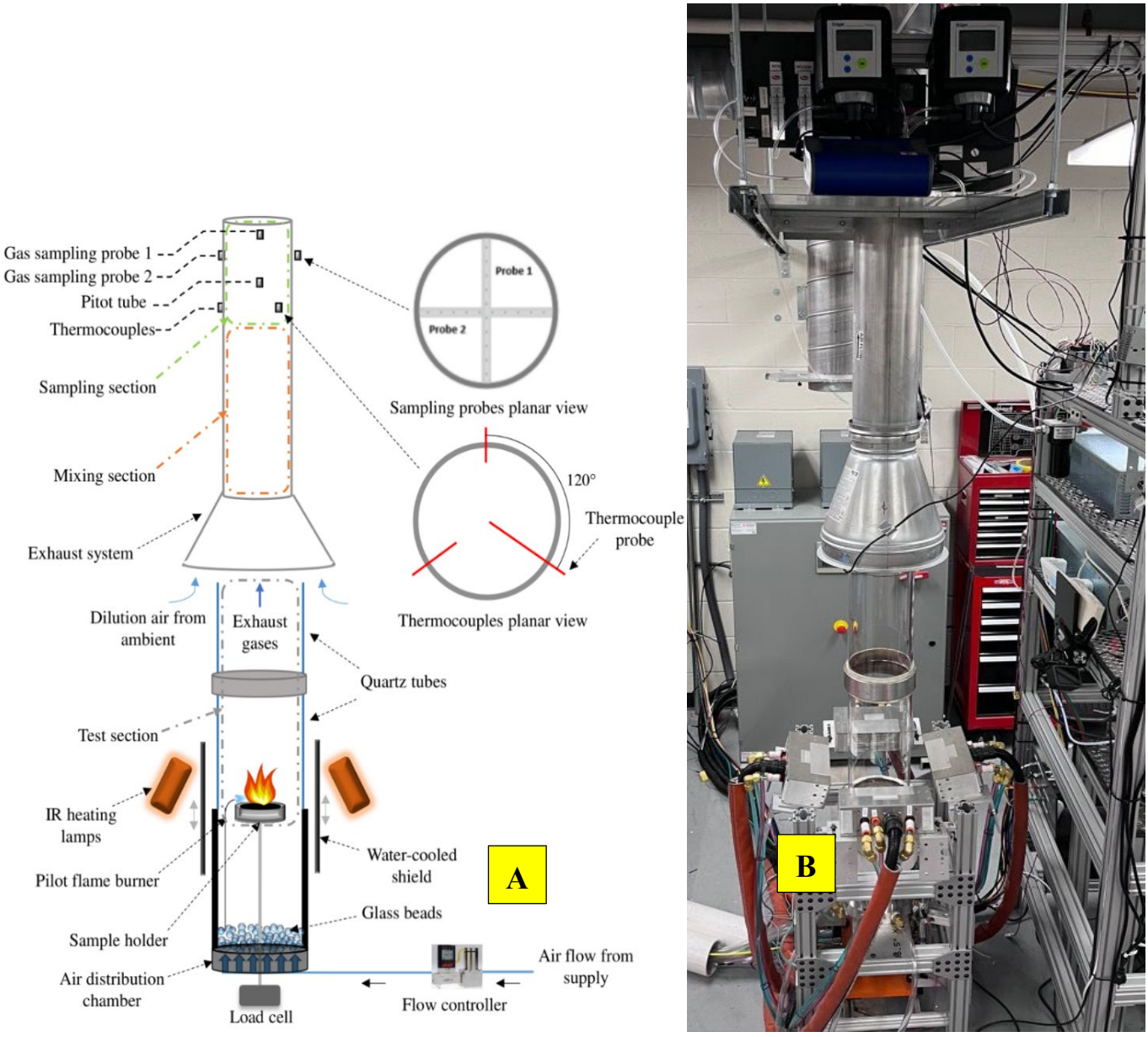


Figure 1. A: Schematic of FPA used in current study B: Corresponding operational FPA in lab

The heating initiates pyrolysis of the sample and the produced gases are ignited with an ethylene/air premixed pilot flame. Once the sample is ignited, combustion proceeds within the quartz tubes. The combustion products exiting the open end of the quartz tubes are rapidly mixed with cool ambient air in the exhaust system to reduce the product concentrations by 30 to 75 times and terminate the combustion reactions.

An averaging pitot tube connected to a pressure transduced and three 0.245-mm-diameter sheathed K-type thermocouples (only one thermocouple is specified in the standard) measure the flow rate and temperature, respectively, within the exhaust duct. The thermocouples are positioned within the same plane perpendicular to the duct's axis at three distinct radial locations, as illustrated in Figure 1. The flow rate in the duct can be adjusted from 0.10 to 0.25 $m^3\ s^{-1}$ (duct flow rate in the range of 0.1 to 0.3 $m^3\ s^{-1}$ is specified in the standard). Controllable duct flow rate allows for adjusting the product concentrations to ensure they remain within the operational range of analytical instrumentation. The duct also contains two sampling probes that are used to measure the concentrations of $CO_2$, CO, $O_2$, unburned total hydrocarbons (THC), HCN, HBr, HCl, NO, and particulate matter (PM) in the exhaust flow. A standard FPA uses one sampling probe to measure $CO_2$, CO, and $O_2$ concentrations, while PM is quantified within the duct using the laser extinction method. A more detailed description of the FPA used in the current study can be found in (Chaffer, 2021; Roy, 2022).

## 2.2 Sampling lines and measurement sensors

As detailed in Section 2.1 and Figure 1, the FPA's exhaust system is equipped with two gas sampling probes positioned at different heights, 76 mm apart, and perpendicular to each other. Each probe features 10 evenly distributed, 1.18-mm-diameter orifices with sampling conducted from both ends of each probe. Gas sampling probes 1 and 2 connect to sampling lines 1 and 2, respectively.

The gas sampling line 1, a schematic of which is shown in Figure 2, delivers a gas sample to the gas analyzer (CAI 700LX NDIR/$O_2$). This analyzer measures $CO_2$ and CO molar or volume fractions using non-dispersive infrared (NDIR) sensors and $O_2$ molar or volume fraction using a paramagnetic sensor. Prior to the analyzer, the sampling flow is filtered, and moisture is completely removed using a chiller that cools down the flow to 5 °C and passes through a pack of mesh Drierite.

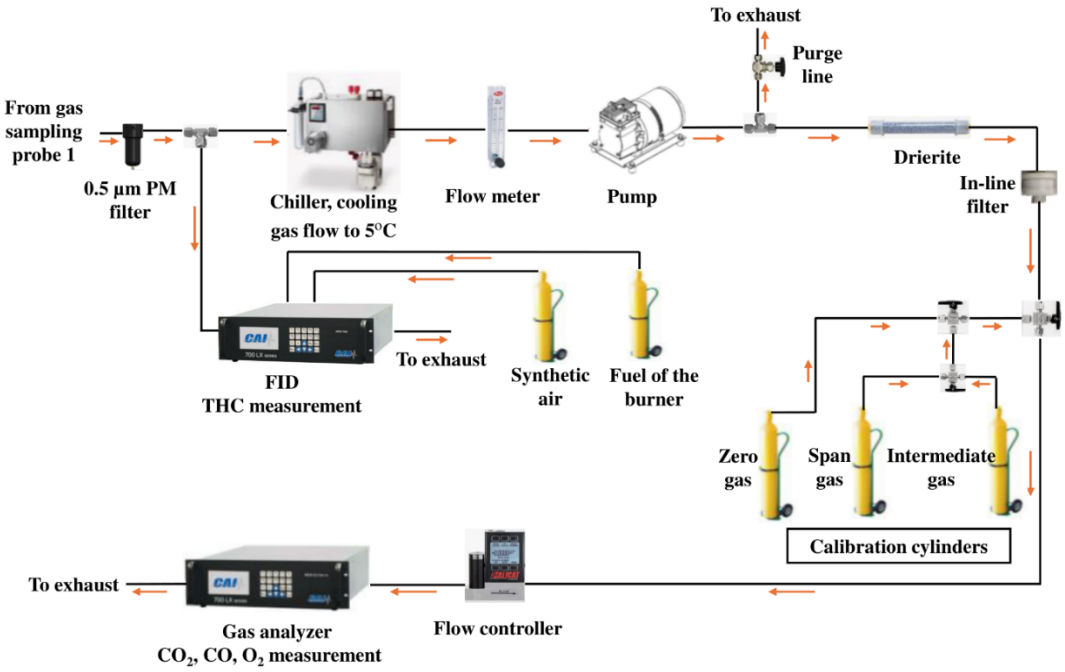


Figure 2. Gas sampling line 1

THC was initially measured using an NDIR sensor (Edinburgh Gascard NG), but this approach did not provide sufficient accuracy at low concentrations. Alternative measurement methods were evaluated, and a flame ionization detector (FID) (FID, CAI 700LX) was selected as the more reliable option. The FID, installed in sampling line 1, is used to quantify THC on a molar basis. The FID detects molecules containing C-H bonds in the sample flow passing through a hydrogen flame (Hinshaw, 2005) and is known to be highly linear with respect to hydrocarbon concentration.

The pump in sampling line 1 draws a total flow rate of 10 liters per minute (LPM). From this flow, 6.8 LPM is purged, while 2 LPM is directed to the gas analyzer, and 1.2 LPM is delivered to the FID. A valve on the purge line is used to regulate line pressure. This configuration ensures fast transport of the sample to the analyzers and stable flows through the analyzers.

The gas sampling line 2, a schematic of which is shown in Figure 3, is designated for the measurement of PM, acid gases, and NO. PM is measured using a TSI DustTrak™ model 8530, which operates based on the light scattering principle (P. B. Keady, 2000). In the standard FPA, PM is measured via light extinction, a method known for significant signal noise and large uncertainties when translating measured data to actual yields (Tian, Gao, Balusamy, & Hochgreb, 2015). In contrast, the light scattering method offers a high signal-to-noise ratio, rapid response, and more accurate measurement at low concentrations (Chen, et al., 2018; Han, Liu,

Jiang, Wang, & Xu, 2021). The DustTrak™ photometric analyzer estimates particulate concentration from the intensity of scattered light, which depends on particle size distribution and refractive index. Because these optical properties vary among combustion products from different fuels, the instrument must be calibrated specifically for the PM generated by each material. This calibration is performed gravimetrically using filter-based measurements, allowing the scattered-light signal to be accurately converted to PM mass concentration.

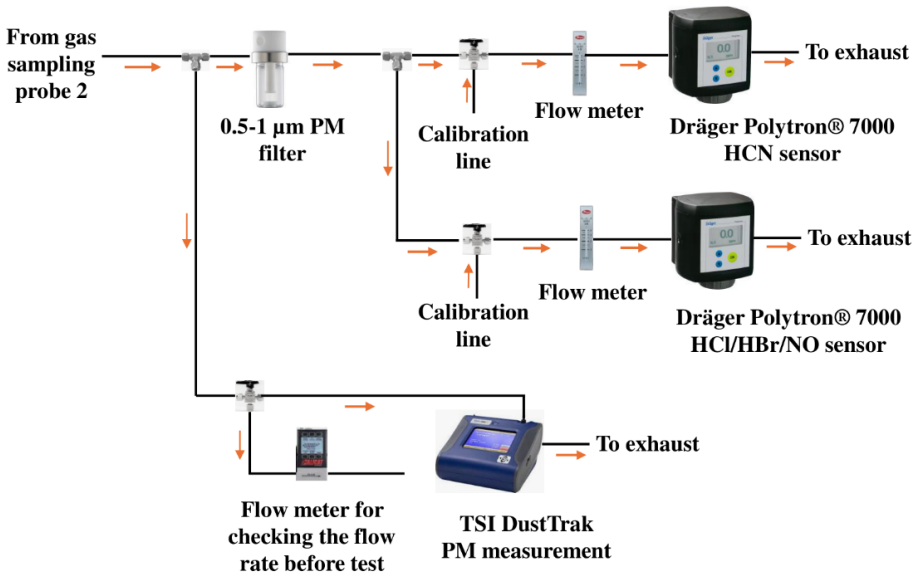


Figure 3. Gas sampling line 2

The deposition of PM inside the exhaust duct was found to be negligible. However, a measurable amount of PM accumulated on the inner surfaces of the quartz tubes. To measure the deposited PM mass on the quartz tube, the deposited particles were carefully brushed from the inner surface into a weighing dish, placed in a desiccator at 15% relative humidity for 24 hours, and then weighed. Further details on the PM deposition fraction and gravimetric calibration are provided later in section 2.5.1.

Dräger Polytron® 7000 transmitters equipped with electrochemical sensors are used to measure HCN, HCl, HBr, and NO molar or volume fractions. For the materials tested in this study, poly(methyl methacrylate) (PMMA) and oriented strand board (OSB), only the HCN and NO sensors were utilized. Flow rates directed to the DustTrak™, and each electrochemical sensor are set at 3 LPM and 1.5 LPM, respectively. Flow meters positioned before each instrument continuously monitor these flow rates, ensuring adherence to the specified settings. A Polytetrafluoroethylene (PTFE) filter in a Pyrex glass housing was installed in the acid gas

measurement line to remove the PM while minimizing absorption of acid gases. The filter had a pore size of 0.5–1 μm.

All gas sensor outputs are recorded at a frequency of 5 Hz to enable removal of high frequency noise in subsequent data processing. The delay time of each sensor (defined as the time elapsed between an event occurring at the sample location and the detected reaction of the corresponding sensor) was individually measured and corrected for synchronizing all signals. In addition, a comprehensive cross-sensitivity analysis was performed to assess the potential interference among different gas measurements. In the current work, it was determined that the NO sensor exhibits cross-sensitivity to CO, with a response equivalent to approximately 5 ppm NO per 1000 ppm CO. Therefore, a correction for the presence of CO was performed during the processing of the NO sensor data.

## 2.3 System calibration and verification

All sensors used in the FPA were regularly calibrated, with daily verification checks incorporated into the standard operating procedure. Calibration converts the sensor's electrical output (typically a voltage or milliampere signal) into a physically meaningful value such as gas concentration or pressure. Each analyzer was calibrated using two standard gases: a zero gas (nitrogen, containing none of the target species) and a span gas with a known concentration usually corresponding to approximately 80–90 % of the analyzer's full-scale range (span gas concentration in the current study: 4400 ppm $CO_2$, 500 ppm CO, and 20.97 % $O_2$). These two points define the linear calibration line used to translate the measured voltage or milliampere into concentration or pressure units.

To confirm that the entire measurement system, including the sampling lines, mixing section, and analyzers, was performing accurately, periodic gas-injection tests were conducted. In the injection test, a reference gas of known concentration and flow rate was injected through a small tube positioned at the sample location inside the test chamber, while the quartz-tube and duct flow conditions were maintained as in an actual FPA combustion test. The injected gas was measured by its corresponding analyzer (e.g., CO or $CO_2$ by the gas analyzer, propane by the FID). Because the injected gas flow, duct flow, and gas composition were all known, the expected concentration reaching the analyzers could be calculated and compared with the measured value. The difference between the measured value and the calculated/injected value indicated the overall system accuracy. The complete injection-test procedure and associated calculations are described in Roy (2022).

During the initial gas-injection tests, the gas analyzer consistently underreported CO, $CO_2$, and $O_2$ concentrations compared to the calculated values. The following paragraphs describe the steps taken to identify the cause of this discrepancy and to resolve the issue. First, a calibration-nonlinearity check was performed for the CO, $CO_2$, and $O_2$ analyzer. A calibration nonlinearity check evaluates whether the analyzer's electrical response (voltage or milliampere signal) increases proportionally with the true gas concentration. In an ideal case, the relationship between signal and concentration is perfectly linear — meaning that doubling the gas concentration doubles the measured signal. However, in practice, some analyzers can deviate from this linear behavior.

During the calibration-nonlinearity check, calibration gases of known concentrations (zero, mid-range, and span) were measured by the analyzer. The measured readings were compared to the expected linear response derived from the standard two-point calibration (zero–span). If the analyzer's mid-range reading differs significantly from the expected value, this indicates nonlinearity in the signal–concentration relationship. In this study, the CO and $O_2$ analyzer maintained a linear response, but the $CO_2$ analyzer showed noticeable nonlinearity, meaning its signal did not scale proportionally with actual $CO_2$ concentration, leading to underestimation at mid-range levels.

To correct the calibration-nonlinearity issue, a third calibration point was added for $CO_2$. The daily calibration procedure for the $CO_2$ channel was therefore expanded to include a mid-range calibration gas (1990 ppm $CO_2$) in addition to the standard zero and span gases. This allowed the calibration curve to be represented by two linear segments, one from zero to the mid-range concentration and another from the mid-range to the full-scale concentration. This adjustment effectively removed the mid-range bias and improved the overall accuracy of $CO_2$ measurements in subsequent experiments.

Since the calibration nonlinearity check did not fully explain the previously observed discrepancy between expected and measured concentrations during injection tests, additional steps were taken to improve flow measurement and mixing accuracy. The Pitot tube, used to measure differential pressure and infer volumetric flow rate, was recalibrated through repeated injection tests. These tests produced a revised K-factor (the coefficient used in converting measured pressure difference to flow velocity) that minimized the difference between expected and measured gas concentrations. Additionally, the orifice plate located at the duct entrance, which enhances turbulence and promotes better mixing between the dilution air and combustion products or injected test, was resized from 12 cm to 11 cm in diameter to optimize the mixing conditions within the duct.

The pressure transducer calibration, which converts a voltage signal into a corresponding pressure value, was also reviewed. Instead of relying on a single linear equation for the full range, the manufacturer-provided set of piecewise voltage-to-pressure conversion equations was implemented. This approach improved accuracy at both low and high pressures.

Finally, to achieve more reliable detection of THC, the original NDIR sensor (Edinburgh Gascard NG) was replaced with an FID installed in sampling line 1. The FID provided higher sensitivity and better precision for low THC concentrations than the NDIR analyzer.

Injection tests are repeated periodically to confirm the overall measurement accuracy. The Pitot-tube calibration coefficient is re-checked whenever any physical change is made to the duct system, and daily zero–span (and mid-point for $CO_2$) calibrations are maintained for all analyzers. Each calibration event is documented, including the type and certified concentration of gases used, ensuring traceability and consistency throughout all experimental campaigns.

The DustTrak™ photometric analyzer was zero-calibrated daily using the supplied zero filter in accordance with the manufacturer's instructions. In addition, it was calibrated against gravimetric PM measurements using glass-fiber filters (Zefon 934-AH, 37 mm diameter, 1.5 μm pore size) installed at the analyzer outlet. The ratio of the gravimetrically determined PM mass to the instrument-reported mass was used to establish a calibration factor ($CF_{\mathrm{PM}}$). The resulting calibration factors were 0.41 ± 0.03 for PMMA and 0.29 ± 0.02 for OSB and were found to be independent of the ventilation condition. The detailed calculation of this calibration factor is provided in Section 2.5.1, after the required parameters for this calculation are introduced.

FID was not calibrated using conventional reference gases such as methane or propane. Instead, its response was corrected for the specific sensitivity to each fuel's pyrolyzate through dedicated pyrolysis experiments. This approach ensured that the measured THC concentrations accurately reflected the chemical composition of gases evolved from PMMA and OSB. The details of this correction procedure are presented in Section 2.5.2, after the derivation of the necessary terms such as species yields and mass.

Dräger™ sensors, were calibrated daily using zero gas (pure nitrogen) and span gas (10 ppm HCN, 50 ppm NO).

## 2.4 Constant-*GER* experiment procedure

Fire ventilation conditions are often characterized by a Global Equivalence Ratio (*GER*), which has a significant influence on species yields (Pitts, 1995). *GER* is an extension of a combustion parameter, equivalence ratio or $\phi$, defined as the ratio of the concentration of the gaseous fuel

and oxidizer divided by the same ratio at stoichiometric conditions corresponding to a complete combustion reaction. Unlike $\phi$, which is a local quantity, *GER* represents the average or global ventilation conditions in an enclosure where the fire takes place. *GER* is computed using the ratio of the mass flow of the gaseous fuel into the enclosure divided by the mass flow of the oxidizer (usually oxygen):

$$GER = r_s \frac{\dot{m}_{fuel}}{\left(\dot{m}_{in}\, Y_{O_2}\right)} \qquad 1$$

where $r_s$ is the mass-based stoichiometric oxidizer to fuel ratio, $\dot{m}_{fuel}$ is the mass flow rate of the gaseous fuel into the enclosure, $\dot{m}_{in}$ is the mass flow rate of incoming ventilation gas into the enclosure, and $Y_{O_2}$ is the oxygen mass fraction in the incoming ventilation gas flow. *GER* < 1 represents well-ventilated conditions, while *GER* > 1 represents under-ventilated fire conditions.

According to Equation 1, a constant-*GER* can be maintained, even when $\dot{m}_{fuel}$ significantly varies with time, by varying $\dot{m}_{in}$ in a synchronous manner so that the ratio of these two quantities remains constant. In FPA, $\dot{m}_{fuel}$ is measured and referred to as $MLR^t$ (mass loss rate of the sample at time *t*), while $\dot{m}_{in}^t$ represents the mass flow rate of dry air supplied into the test section at time t, with an oxygen mass fraction $Y_{O_2}$= 0.231. $\dot{m}_{in}^t$ can be regulated using a fast-response programmable mass flow controller (see Figure 1), which provides a capability for maintaining a constant-*GER*.

### 2.4.1 Constant-*GER* test method

Constant-*GER* experiments were designed to maintain a prescribed ventilation condition throughout the combustion process for any solid fuel tested in the FPA. The procedure begins with determining the mass-based stoichiometric oxidizer-to-fuel ratio, $r_s$, from the balanced equation for the complete combustion of the fuel's pyrolyzate with $O_2$ as the oxidizer and $CO_2$ and $H_2O$ as the only products. Once $r_s$ is known, the time-resolved air flow rate ($\dot{m}_{\text{in}}^t$) required to sustain a target *GER* is calculated using the measured mass-loss-rate ($MLR^t$) data from preliminary over-ventilated tests.

In practice, a non-constant-*GER* test is first conducted at a fixed air flow rate sufficiently high to ensure the *GER* remains below the minimum desired constant-*GER* value. The resulting $MLR^t$ curve is then used to compute the air-flow-rate history that would yield the desired constant-*GER* condition through the relation between *GER*, $r_s$, $MLR^t$, and $\dot{m}_{\text{in}}^t$:

$$\dot{m}_{\text{in}}^t = r_s \frac{MLR^t}{\left(GER_{target}\ Y_{O_2}\right)} \qquad 2$$

where $GER_{target}$ is the desired *GER* that the test is designed to maintain as constant. This time series of $\dot{m}_{\text{in}}^{t}$ values is converted into a sequence of mass-flow-controller (MFC) set points, each adjusted at regular intervals (10 s in this study) to allow sufficient response time for the system. For subsequent tests at higher *GER* values, the $MLR^{t}$ data obtained from the immediately lower-*GER* experiment are used to define the new MFC set-point profile, ensuring that each condition builds on experimentally observed burning behavior.

To promote stable ignition and full flame development, the constant-*GER* control is not applied at the very beginning of the test. Instead, the air flow rate is held constant at an over-ventilated value (200 SLPM) from the start of heating until about 15 s after ignition, after which the programmed *GER* control sequence begins.

### 2.4.2 Air entrainment evaluation and flow control limitations

During the design of the constant-*GER* experiments, a critical issue was identified: air entrainment into the quartz tube from its open top at low air flow rates. This unintended backflow of ambient air was unacceptable because it introduced additional oxygen into the combustion zone, altering the actual *GER* and compromising the test's control and repeatability.

To determine the minimum flow rate required to prevent this backflow, a series of diagnostic tests were performed. In these tests, $N_2$, rather than air, was introduced into the quartz tube and test section at various flow rates, while $O_2$ concentration was monitored at several locations inside the quartz tube. $O_2$ presence served as an indicator of the surrounding air entrainment from the top of the quartz tube.

The sampling tubing was first inserted into the predetermined locations inside the quartz tube (Figure 4) before each measurement, to prevent disturbing the flow field. To ensure that no ambient air trapped inside the tubing was drawn into the analyzer at the start of sampling, the tubing was pre-flushed with $N_2$ prior to insertion. Once the tubing was in position, $N_2$ was flowed through the test section for approximately 2 minutes to purge any remaining air and allow the $O_2$ readings to stabilize prior to each run.

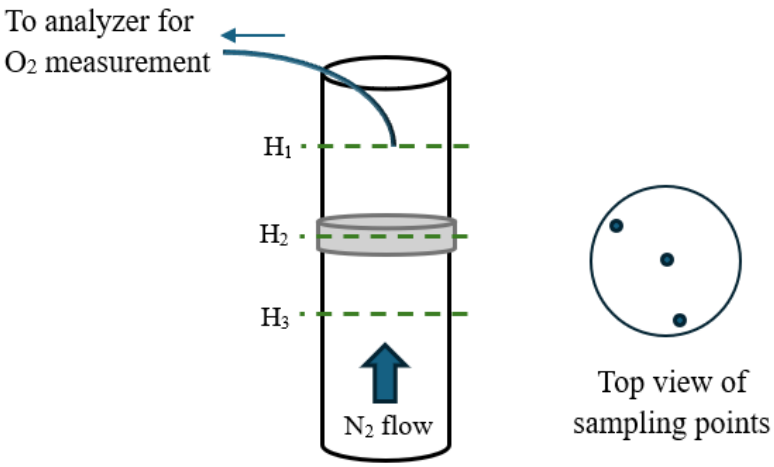


Figure 4. Air-entrainment test used to quantify air backflow at different $N_2$ flow rates

Measurements were taken at three vertical heights, $H_1$, $H_2$, and $H_3$, located approximately 15 cm, 30 cm, and 45 cm below the top opening of the quartz tube, respectively. At each height, three sampling points were used: two near the wall and one at the centerline. Sampling was conducted for one minute at each point, and the mean $O_2$ concentration across the three locations was calculated for each height.

The results are summarized in Table 1. $O_2$ concentrations below 5% were considered acceptable, indicating negligible air entrainment. At a flow rate of 75 SLPM, oxygen levels below height $H_1$ remained under this threshold, confirming that backflow was effectively suppressed in this region. Accordingly, during PMMA combustion experiments at the highest *GER* conditions that the air flow rates reached 75 SLPM, the flame height was carefully monitored to ensure it remained well below $H_1$—maintaining stable and well-defined ventilation throughout the test. Because the quartz tube gradually became obscured by soot deposition during burning, direct visual monitoring from outside was not feasible. Therefore, the flame height was tracked using a camera installed inside the exhaust duct, which provided a clear line of sight into the test section.

Table 1. $O_2$ concentration inside quartz tube at different sampling locations and $N_2$ flow rates

| | **$O_2$ concentration, %** | | |
|---|---|---|---|
| | **$N_2$: 50 SLPM** | **$N_2$: 75 SLPM** | **$N_2$: 100 SLPM** |
| H1 | 10.8 ±2.5 | 6.1 ± 3.4 | 0.4 ± 0.2 |
| H2 | 5.1 ± 0.7 | 0.5 ± 0.4 | 0.2 ± 0.1 |

| | **$O_2$ concentration, %** | | |
|---|---|---|---|
| | **$N_2$: 50 SLPM** | **$N_2$: 75 SLPM** | **$N_2$: 100 SLPM** |
| H3 | 1.5 ± 0.2 | 0.6 ±0.2 | 0.0 ± 0.0 |

For the OSB experiments, where target *GER* values required air flow rates well below the 75 SLPM threshold, additional tests were performed with a metal cap placed over the top of the quartz tube shown in Figure 5. The cap's geometry (76.2 mm opening diameter, 39 mm height) was designed to reduce air entrainment while allowing exhaust flow. $O_2$ measurements taken at several heights inside the quartz tube and the results are listed in Table 2. The results confirmed that, with the cap in place, $O_2$ concentrations remained below 5 % even at 25 SLPM, validating the effectiveness of this design for under-ventilated conditions. All OSB experiments were performed using the cap on top of the quartz tube.

Table 2. $O_2$ concentration inside quartz tube at different sampling locations and $N_2$ flow rates with cap installed on quartz tube

| | **$O_2$ concentration, %** | | | |
|---|---|---|---|---|
| | $N_2$: 20 SLPM | $N_2$: 25 SLPM | $N_2$: 50 SLPM | $N_2$: 75 SLPM |
| $H_1$ | 5.8 ± 1.2 | 3.1 ± 1.1 | 2.2 ± 0.3 | 0.3 ± 0.2 |
| $H_2$ | 4.6 ± 1.1 | 2.5 ± 0.4 | 0.8 ± 0.2 | 0.2 ± 0.1 |
| $H_3$ | 4.4 ± 1.2 | 2.2 ± 0.4 | 0.5 ± 0.1 | 0.2 ± 0.1 |

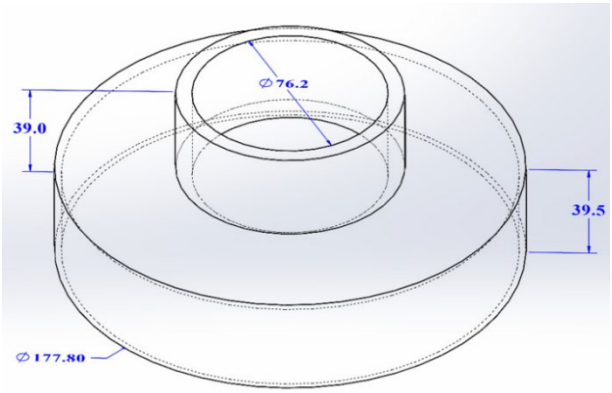


Cap technical drawing, dimensions in millimeters


Figure 5. Removable cap used in OSB experiments to minimize air entrainment at top of quartz tube

### 2.4.3 Implementation for PMMA and OSB

In this study, constant-*GER* experiments were designed by first calculating the mass-based stoichiometric oxidizer-to-fuel ratio, $r_s$, from the balanced complete-combustion equation for PMMA pyrolyzate (with $O_2$ as the oxidizer and only $CO_2$ and $H_2O$ as products). This value was found to be $r_s = 0.52$. All PMMA tests were designed at 75 kW m$^{-2}$ heat flux. The selected heat flux of 75 kW m$^{-2}$ was sufficiently high to allow both over- and under-ventilated regimes to be explored in later tests without reducing the airflow below 75 SLPM. However, for the highest *GER* of PMMA test matrix (*GER* = 1.96), the air flow rate was lower than 75 SLPM for a portion of the test and that part was not considered in the analysis of the results.

A preliminary experiment was performed by burning a PMMA sample at a set radiant heat flux of 75 kW m$^{-2}$ while supplying a constant 300 SLPM of air. Under these conditions, the test remained highly over-ventilated (*GER* < 0.6 at all times). This initial test was repeated three times. The resulting $\dot{m}_{fuel}^{t}$ ($MLR^t$) histories were averaged and used to compute the time-dependent air-flow rate, $\dot{m}_{in}^{t}$, needed to maintain the first target *GER* = 0.63. The computed $\dot{m}_{in}^{t}$ profile was then converted into a sequence of MFC set-points. Each set-point was held for 10 s to ensure adequate response time of the MFC. This procedure is illustrated in Figure 6. In this figure, *t* denotes the time after the drop of the shield.

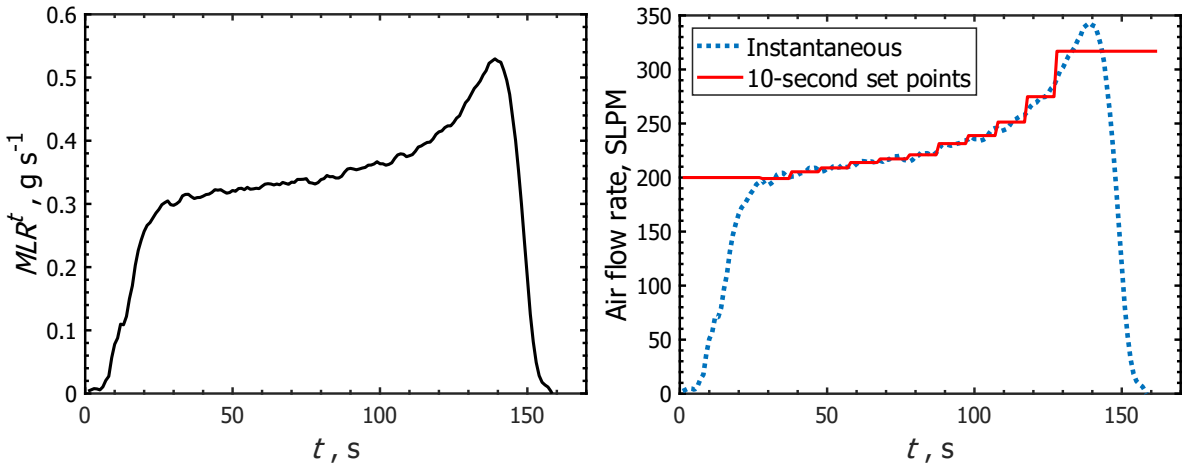


Figure 6. Average $MLR^t$ and corresponding air flow rate
*Required to maintain constant-GER of 0.63 for black cast PMMA subjected to 75 kW m$^{-2}$ of set radiant heat flux*

For higher *GER* values, the required air flow set-point histories were generated in the same way but using the $MLR^t$ data from the immediately preceding constant-*GER* test. For example, the $MLR^t$ data obtained at *GER* = 0.63 were used to compute the airflow profile for *GER* = 1.11; those collected at *GER* = 1.11 were then used for the next *GER* level, and so on.

Finally, as shown in Figure 6, constant-*GER* conditions were not applied from the beginning of each test. Instead, the air flow was held at 200 SLPM from ignition until 15 s afterward to allow the flame to develop fully and uniformly cover the sample surface before transitioning into the constant-*GER* control sequence.

For OSB, the same constant-*GER* framework was applied, but two practical adjustments were necessary due to OSB's different burning characteristics. First, compared to PMMA tests, a higher radiant heat flux of 95 kW m$^{-2}$ and a larger sample area were used to ensure sufficient mass-loss rates for exploring high-*GER* conditions. Second, OSB tests frequently required air flow rates below the 75-SLPM threshold where air entrainment would normally occur. To operate in this regime without compromising ventilation control, a removable cap was installed on top of the quartz tube as explained in the previous section. Therefore, the air flow rates were as low as 25 SLPM for the highest *GER*.

The stoichiometric ratio for OSB pyrolyzate, calculated from its complete combustion equation, was $r_s = 0.872$, and this value was used to generate the corresponding constant-*GER* airflow profiles. The compositions of the PMMA and OSB pyrolyzates are discussed later in Section 2.6.

## 2.5 Calculation of species yields

During both pyrolysis and combustion, the solid sample thermally decomposes and loses mass at a rate $MLR^t$, generating a gaseous pyrolyzate. In combustion tests, this pyrolyzate mixes with the incoming oxidizer and reacts to form multiple product species whose concentrations—and hence mass generation or consumption rates—vary continuously with time. Thus, both the decomposition of the solid and the formation of gas-phase products are inherently time-resolved processes, and the mass lost from the solid at any moment corresponds to the mass generated or consumed in the gas phase.

All analyzer signals and load-cell measurements are recorded at 5 Hz, providing time-resolved species concentrations and sample mass, respectively. The species concentrations are converted into instantaneous mass generation (or consumption) rates, $\dot{m}_i^t$, while the solid-phase mass measurements are used to determine the instantaneous mass-loss rate, $MLR^t$. To reduce high-frequency noise associated with the load cell and to maintain a consistent time resolution across all measurements, all recorded signals are temporally binned by averaging every five consecutive data points. This produces smoothed, 1 Hz datasets suitable for subsequent analysis.

After binning, the instantaneous mass-loss rate is calculated using a backward finite-difference approximation:

$$MLR^t = -\frac{m(t) - m(t-1)}{1\ \text{s}} \tag{3}$$

where $m(t)$ is the binned sample mass at time $t$. The negative sign ensures that $MLR^t$ is positive when mass is lost from the sample. To compute the total mass of each species generated or consumed over a selected portion of the experiment, two user-defined integration time limits, $t_1$ and $t_2$, are specified. These limits may correspond to any interval of interest.

The yield of species $i$ is then defined as the ratio of the total mass of that species generated (or consumed) between two user-defined integration time limits $t_1$ and $t_2$, to the total mass of solid fuel gasified during the same interval:

$$Yield_i = \frac{\int_{t_1}^{t_2} \dot{m}_{i,generated/consumed}^t dt}{\int_{t_1}^{t_2} MLR^t\, dt} \tag{4}$$

Here, $MLR^t$ is the mass loss rate of the sample at time *t*, and $\dot{m}_{i,generated/consumed}^t$ is the mass generation/consumption rate of species *i* at time *t*. In the FPA standard, $\dot{m}_{i,generated/consumed}^t$ is defined as (ASTM International, 2019):

$$\dot{m}^t_{i,generated/consumed} = \dot{m}^t_{duct} \frac{MW_i}{MW_{air}} (X^t_i - X^0_i) \quad 5$$

where $\dot{m}^t_{duct}$ is the mass flow rate in the duct at time *t*. $X^0_i$ and $X^t_i$ are the measured molar or volume fraction of species *i*. A superscript "0" indicates values measured prior to the drop of the shield; a superscript "*t*" indicates time dependent values at time *t* after the drop of the shield. $MW_i$ and $MW_{air}$ are the molecular weight of species *i*, and air, respectively.

In the ASTM standard (ASTM International, 2019), $\dot{m}^t_{duct}$ (in kg $s^{-1}$) is obtained using the following equation based on the assumption that the mixture in the duct is essentially air:

$$\dot{m}^t_{duct} = A_{duct} K \sqrt{2\,\Delta P^t \frac{353\,P^t_{duct}}{101{,}000\,T^t_{duct}}} \quad 6$$

In this equation, $A_{duct}$ is the duct cross sectional area in $m^2$; *K* is the dimensionless flow coefficient of the pitot tube; $\Delta P^t$ is the pressure differential across averaging pitot tube in the duct in Pa; $P^t_{duct}$ is the absolute atmospheric pressure in the duct in Pa. $P^t_{duct}$ is calculated as the ambient pressure minus the pressure difference recorded by the pitot tube. $T^t_{duct}$ is the gas temperature in the duct, in K, which is measured by one thermocouple located in the duct. Here, 101,000 Pa is the reference pressure specified in the FPA standard for calculating the duct flow rate and 353 kg K $m^{-3}$ is the density of air at atmospheric pressure multiplied by $T^t_{duct}$.

In the current work, the mass generation/consumption rate of each species was computed from the raw signals using a modified set of equations that relax some of the assumptions used in the standard formulation and thus deliver a higher accuracy. The mass generation/consumption rate was defined as follows:

$$\dot{m}^t_{i,generated/consumed} = \dot{m}^t_{duct}\, MW_i \left( \frac{X^t_i}{MW^t_{duct}} - \frac{X^0_i}{MW^0_{duct}} \right) \quad 7$$

Unlike in the standard approach where $MW_i$ is divided by the molecular weight of air, in the current formulation $MW_i$ is divided by the molecular weight of the gas mixture in the duct, $MW^t_{duct}$ at specific time. $\dot{m}^t_{duct}$ is calculated using the Bernoulli equation (Gerhart, Hochstein, & Gerhart, 2020) and expressed as:

$$\dot{m}^t_{duct} = A_{duct} K \sqrt{2\,\Delta P^t \frac{MW^t_{duct}\,P^t_{duct}}{R\,T^t_{duct}}} \quad 8$$

Here, *R* is the universal gas constant in units of J $mol^{-1}$ $K^{-1}$; $P^t_{duct}$ is the absolute pressure in the duct obtained by measuring the ambient pressure before a test and subtracting the differential

pressure measured by the pitot tube in units of Pa; and $T_{duct}^{t}$ is the gas temperature determined by averaging the signals of three thermocouples in the duct in units of K.

For HCN, and NO, $X_i^0$ and $X_i^t$ used in Equation 7 are obtained directly from the detector/sensor data after applying an appropriate calibration. For THC, the sensor signal was also initially processed using Equation 7 with propane's molecular weight used as the reference molecular weight. The resulting $\dot{m}_{i,generated/consumed}^{t}$ was subsequently corrected to account for the difference in the sensitivity between propane and PMMA or OSB pyrolyzate. The FID was found to be about 0.5 times as sensitive to PMMA pyrolyzate and 0.2 times as sensitive to OSB pyrolyzate. The derivation of the FID correction factors is described in Section 2.5.2.

For $CO_2$, CO, and $O_2$ signals, an additional correction is required to compensate when all moisture present in the duct is removed from the CAI 700LX analyzer flow (see Figure 2). The molar or volume fractions of these gases in the duct can be expressed as:

$$X_i^t = \left( \frac{n_{total-\mathrm{H2O}}^t}{n_i^t} + \frac{n_{\mathrm{H2O}}^t}{n_i^t} \right)^{-1} \qquad 9$$

Here *i* represents $CO_2$, CO, or $O_2$; $n_i^t$ is the number of moles of species *i*; $n_{H2O}^t$ is the total number of moles of gaseous $H_2O$ in the duct; and $n_{total-H2O}^t$ is the total number of moles of all gases excluding $H_2O$. The first term inside parentheses is the reciprocal of the gas analyzer measurement, $\frac{1}{X_{i,measured}^t}$, while the second term can be expressed as:

$$\frac{n_{\mathrm{H2O}}^t}{n_i^t} = \frac{\frac{n_{\mathrm{H2O}}^0}{n_{\mathrm{CO2},comb}^t} + \frac{n_{\mathrm{H2O},comb}^t}{n_{\mathrm{CO2},comb}^t}}{\frac{n_i^t}{n_{\mathrm{CO2},comb}^t}} \qquad 10$$

where $n_{\mathrm{H2O}}^0$ and $n_{\mathrm{H2O},comb}^t$ represent the number of moles of water vapor that entered the duct from the ambient and number of moles of water vapor produced in the combustion process respectively; and $n_{\mathrm{CO2},comb}^t$ is the number of moles of $CO_2$ produced in the combustion process.

The terms on the right-hand side of Equation 10 are estimated using the gas volume fractions measured by the gas analyzer (indicated by a subscript "*measured*" in equations 11 to 13) and the ratio of the number of hydrogen and carbon atoms $\left(\frac{H_{atoms}}{C_{atoms}}\right)$ in the gaseous pyrolyzate. The pyrolyzate composition will be discussed in the next section. Using these quantities, the terms in Equation 10 may be expressed in the following form:

$$\frac{n^0_{\mathrm{H2O}}}{n^t_{\mathrm{CO2},comb}} \approx \frac{X^0_{\mathrm{H2O}}}{X^t_{\mathrm{CO2},measured} - X^0_{\mathrm{CO2},measured}} \tag{11}$$

$$\frac{n^t_i}{n^t_{\mathrm{CO2},comb}} = \frac{X^t_{i,measured}}{X^t_{\mathrm{CO2},measured} - X^0_{\mathrm{CO2},measured}} \tag{12}$$

$$\frac{\dfrac{n^t_{\mathrm{H2O},comb}}{n^t_{\mathrm{CO2},comb}}}{\approx \dfrac{\frac{1}{2}\left(\frac{H_{atoms}}{C_{atoms}}\right)\left(\left(X^t_{\mathrm{CO2},measured} - X^0_{\mathrm{CO2},measured}\right) + \left(X^t_{\mathrm{CO},measured} - X^0_{\mathrm{CO},measured}\right)\right)}{X^t_{\mathrm{CO2},measured} - X^0_{\mathrm{CO2},measured}}} \tag{13}$$

Here $X^0_{\mathrm{H2O}}$ represents the molar or volume fraction of water vapor in the ambient, which is computed from measured relative humidity, ambient pressure, and saturated vapor pressure at ambient temperature. While Equations 11 to 13 do not take into account the removal of moisture from the analyzer flow, they provide a sufficiently accurate input for the calculation of $X^t_i$ to make the error in $\dot{m}^t_{i,generated/consumed}$ associated with the removal of moisture significantly smaller than those associated with instrumental uncertainty of the gas analyzers (on the order of ±1–2% of full scale, depending on species and measurement range). Equation 13 relies on the assumption that the $H_2O$ produced during combustion originates from the molecules of the gaseous pyrolyzate that oxidize to CO and/or $CO_2$ and that all hydrogen in these molecules is converted to $H_2O$.

Equations 9 to 13 provide an accurate assessment $X^t_i$ for $CO_2$, CO, and $O_2$, which analyzer readings are affected by the removal of $H_2O$ from the sampling stream. The accuracy is based on the fact that these calculations require fewer simplifying assumptions. Similar corrections are performed to compute $X^0_i$ for these gases from the analyzer data collected before the drop of the shield (Roy, 2022). $MW^t_{duct}$, required in the current formulation for the calculation of the mass generation/consumption rate of every species, is computed by taking into account the contributions from major species ($CO_2$, CO, $O_2$, and $H_2O$) and assuming $N_2$ balance:

$$MW^t_{duct} = \left(\sum\nolimits_{i=\mathrm{CO2,CO,O2}} \left(MW_i X^t_{i,measured}\right) + MW_{N2}\left(1 - \sum\nolimits_{i=\mathrm{CO2,CO,O2}} X^t_{i,measured}\right)\right)\left(1 - X^t_{\mathrm{H2O}}\right) + MW_{\mathrm{H2O}} X^t_{\mathrm{H2O}} \tag{14}$$

Here $X_{\mathrm{H2O}}^{t}$ is the molar or volume fraction of water vapor in the duct at time t computed as:

$$X_{\mathrm{H2O}}^{t} = \frac{n_{\mathrm{H2O}}^{t}}{n_{\mathrm{CO2}}^{t}} X_{\mathrm{CO2}}^{t} \quad 15$$

where $\frac{n_{\mathrm{H2O}}^{t}}{n_{\mathrm{CO2}}^{t}}$ is determined from Eq. 10 with *i* representing $CO_2$. The mass generation rate of PM was computed somewhat differently from that of gases because TSI DustTrak™ measures the mass concentration of PM, $C_{\mathrm{PM}}^{t}$, expressed in kg m$^{-3}$. The mass generation rate of PM is obtained as:

$$\dot{m}_{\mathrm{PM},\,generated}^{t} = \frac{1}{1 - f_{dep}} CF_{PM}\, C_{\mathrm{PM}}^{t} \frac{\dot{m}_{duct}^{t}}{MW_{duct}^{t}} \frac{R\, T_{duct}^{t}}{P_{duct}^{t}} \quad 16$$

where $f_{dep}$ represents the fraction of PM deposited on the quartz tubes, used to correct the measured PM concentration, and $CF_{PM}$ is the DustTrak™ calibration factor determined experimentally by comparing light-scattering readings with gravimetric PM measurements for each solid fuel.

Because $CF_{PM}$ and $f_{dep}$ depend on the fuel type and/or experimental conditions, their determination and application are described in the following subsections, together with the corresponding procedure used to correct the THC signal.

### 2.5.1 Particulate matter corrections

The DustTrak™ photometric analyzer estimates particulate concentration based on the intensity of scattered light, which depends on particle size distribution and refractive index. Because these optical properties vary between combustion products of different fuels, the instrument response must be calibrated specifically for PM produced by each material.

In this study, DustTrak™ was calibrated against gravimetric measurements obtained during combustion tests of PMMA and OSB. A glass-fiber filter was installed at the DustTrak™ outlet to collect the total PM emitted during each experiment. Before each test, the filters were conditioned in a desiccator maintained at approximately 15% relative humidity for at least 24 hours, then pre-weighed using an analytical balance. After the test, the filters were reconditioned under the same conditions and re-weighed to determine the net mass of PM collected. This procedure minimized the influence of absorbed moisture on the measured filter mass.

The gravimetric PM collection was conducted during standard FPA combustion experiments, using an air flow rate of 200 SLPM and incident heat fluxes of 50 kW m$^{-2}$ and 95 kW m$^{-2}$ for PMMA and OSB, respectively. Since the DustTrak™ outlet flow rate where the filter is placed

was 2 LPM (equivalent to $3.33 \times 10^{-5}$ $m^3$ $s^{-1}$), the total mass of PM reported by the instrument was computed as:

$$m_{PM,measured} = 3.33 \times 10^{-5} \int_0^{t_{end}} C_{\mathrm{PM}}^{t} \, dt \quad (17)$$

where $C_{\mathrm{PM}}^{t}$ is the instantaneous PM mass concentration (kg $m^{-3}$) measured by DustTrak ™and $t_{\mathrm{end}}$ is the experiment duration.

The DustTrak™ calibration factor ($CF_{\mathrm{PM}}$) was determined as the ratio of the gravimetrically collected mass to the total mass reported by the instrument:

$$CF_{PM} = \frac{m_{PM,collected\ on\ filter}}{m_{PM,measured}} \quad (18)$$

This calibration factor allows accurate conversion of DustTrak™ light-scattering readings into true particulate mass concentrations. The resulting calibration factors were 0.41 ± 0.03 for PMMA and 0.29 ± 0.02 for OSB, reflecting the optical and physical differences in particulates generated from each material. These calibration factors were determined during constant-*GER* experiments, and the values obtained under different ventilation conditions were all within the reported uncertainty ranges. Therefore, the calibration factors are considered independent of the ventilation condition.

In addition to the gravimetric calibration, losses of particulate matter due to deposition on the inner surfaces of the quartz tubes were also quantified. The PM deposition fraction was defined as:

$$f_{dep} = \frac{m_{\mathrm{PM},deposited}}{m_{\mathrm{PM},DustTrak} + m_{\mathrm{PM},deposited}} \quad (19)$$

where $m_{PM,DustTrak}$ is the PM mass recorded by the DustTrak™ and is obtained by integrating Equation 16 over the entire test duration before applying the deposition correction, and $m_{PM,deposited}$ is the mass recovered from the quartz tubes (and from the cap in the case of OSB).

For PMMA, the deposited portion was small, about 0.091 ± 0.025 of the total PM and showed little variation with ventilation conditions. In contrast, for OSB, the deposition fraction changed noticeably with the *GER*. Therefore, separate correction factors were applied for each constant-*GER* condition, as summarized in Table 3.

Table 3. PM deposition fraction for OSB at different *GER*s.

| $GER$ | $f_{dep}$ |
|---|---|
| 0.5 | 0.260 ± 0.018 |
| 0.98 | 0.424 ± 0.014 |
| 1.51 | 0.299 ± 0.019 |

### 2.5.2 Total hydrocarbons corrections

In this study, the response of FID was corrected using gaseous pyrolyzate generated directly from solid fuel samples.

For PMMA, the calibration procedure involved pyrolysis of the sample under an incident heat flux of 50 kW $m^{-2}$ in an anaerobic environment created by flowing 100 SLPM of $N_2$ through the FPA quartz tubes. During these pyrolysis tests, the gas analyzer and FID simultaneously measured the concentrations of $CO_2$, CO, $O_2$, and THC. However, only the THC channel showed measurable signals for PMMA pyrolysis.

The calibration factor for PMMA, $CF_{\text{THC, PMMA}}$, was calculated as:

$$CF_{\text{THC},PMMA} = \frac{m_{pyrolyzed\ \text{PMMA}}}{m_{measured\ \text{THC}}} \qquad 20$$

where $m_{measured\ \text{THC}}$ and $m_{pyrolyzed\ \text{PMMA}}$ represent the total mass of measured hydrocarbons and the total mass of PMMA decomposed, respectively. Each was determined by integrating the corresponding mass generation or loss rates ($\dot{m}^t_{\text{THC}}$ from Equation 7) and $MLR^t$) over the duration of the pyrolysis test.

This method provides a more realistic calibration than using standard gases such as methane or propane, because the chemical composition of the solid fuel pyrolyzate more closely resembles the incomplete combustion products detected by the FID.

For OSB, similar pyrolysis experiments were performed at an incident heat flux of 95 kW $m^{-2}$ and a $N_2$ flow rate of 100 SLPM. Unlike PMMA, the OSB pyrolysis products contained noticeable amounts of CO and $CO_2$, which were included in the calibration factor calculation. Species measurements were obtained using the same analyzers and procedures described previously. The THC calibration factor for OSB was defined as:

$$CF_{\mathrm{THC,OSB}} = \frac{m_{pyrolyzed\ \mathrm{OSB}} - m_{\mathrm{CO2}} - m_{\mathrm{CO}}}{m_{measured\ \mathrm{THC}}} \quad (21)$$

where $m$ denotes the total mass of each species, obtained by integrating its mass generation rate over the duration of the pyrolysis test.

The resulting calibration factors were $2.03 \pm 0.03$ for PMMA and $5.1 \pm 0.1$ for OSB. It should be noted that in the OSB pyrolysis tests, the product yields increased during the initial phase and later stabilized at a nearly constant level. The steady-state region of this plateau was used to determine the species masses and calculate $CF_{\mathrm{THC,\ OSB}}$. This behavior for OSB pyrolysis is discussed in more detail later in the following section.

## 2.6 Composition of solid-fuel pyrolyzates and produced THC

The elemental composition of the pyrolyzate and the corresponding THC is required for balancing the combustion reaction of the fuel vapor, which is needed for calculating the heat of combustion as discussed in the following section. These compositions are also essential for evaluating the accuracy of the measurement system. This is done by comparing the carbon released in the measured products to the carbon initially present in the pyrolyzate, a check commonly referred to as the carbon balance.

### 2.6.1 Poly(methyl Methacrylate)

PMMA undergoes clean gasification during pyrolysis, producing no measurable solid residue and generating only THC as a detectable gaseous species. Therefore, the composition of its pyrolyzate—and the THC produced during its combustion—was assumed to be identical to the known monomer-based composition of the solid polymer ($CH_{1.6}O_{0.4}$).

In contrast, materials that do not have a well-defined atomic composition and/or produce solid residue upon combustion will require an elemental analysis of the uncombusted solid and/or its post-combustion residue.

### 2.6.2 Oriented strand board

OSB is a charring fuel, leaving behind a solid char residue after flaming combustion. Since this study focuses on measuring products from the flaming combustion phase, an accurate composition of the OSB pyrolyzate is required for calculations. To determine the compositions, the mass-based char yield of OSB was first measured to be $19.1 \pm 0.7\%$. This yield was calculated as the ratio of the mass of char residue remaining after flaming combustion had ceased to the oven-dried sample mass prior to the experiment.

Determining the pyrolyzate composition also requires the elemental compositions of both the original OSB and the resulting char. Therefore, two samples of original OSB and two samples of char were submitted for elemental analysis. Carbon, hydrogen, and nitrogen contents were measured using ASTM D5373 (ASTM International, 2016)) and oxygen content was obtained by difference. Analyses were performed by Intertek Laboratories (Romeoville, IL). The results of the elemental analysis for OSB and its char are summarized in Table 4 and Table 5.

Table 4. Elemental analysis results for OSB
*Two replicate samples were analyzed to assess sample-to-sample variability*

| **Component** | **ASTM test method** | **Mass fraction (% wt.), sample 1** | **Mass fraction (% wt.), sample 2** |
|---|---|---|---|
| Carbon | D 5373 | 50.51 | 49.87 |
| Hydrogen | D 5373 | 6.41 | 6.47 |
| Nitrogen | D 5373 | 0.45 | 0.44 |
| Oxygen | Calculated by difference | 42.20 | 42.81 |
| Sulfur | D 4239 | 0.16 | 0.15 |
| Ash | D 3174 | 0.27 | 0.26 |

Table 5. Elemental analysis results for OSB char

*Two replicate samples were analyzed to assess sample-to-sample variability*

| **Component** | **ASTM test method** | **Mass fraction (% wt.), sample 1** | **Mass fraction (% wt.), sample 2** |
|---|---|---|---|
| Carbon | D 5373 | 91.19 | 91.68 |
| Hydrogen | D 5373 | 1.99 | 2.20 |
| Nitrogen | D 5373 | 1.00 | 0.94 |
| Oxygen | Calculated by difference | 4.58 | 4.03 |
| Sulfur | D 4239 | 0.08 | 0.07 |
| Ash | D 3174 | 1.16 | 1.08 |

The elemental compositions of OSB and its char were converted from mass fractions to molar fractions. After normalization by the number of carbon moles, the resulting empirical formulas were $CH_{1.53}O_{0.64}$ for the original OSB and $CH_{0.28}O_{0.04}$ for the char. These values represent the average compositions of the two samples analyzed. Nitrogen, sulfur, and ash contents were excluded from the final empirical formulas because their contributions were negligible.

To determine the composition of the OSB pyrolyzate, the decomposition reaction was written as:

$$\mathrm{CH_{1.53}O_{0.64}} \rightarrow \mu_p\ \mathrm{C_xH_yO_z} + \mu_{\mathrm{char}}\ \mathrm{CH_{0.28}O_{0.04}} \quad (22)$$

where $\mu_p$ and $\mu_{\mathrm{char}}$ are the molar stoichiometric coefficients of the pyrolyzate and char, respectively. Using the measured char yield of 19.1%, this decomposition balance resulted in a pyrolyzate composition of $CH_{2.2}O_{0.97}$.

Three OSB pyrolysis tests were conducted at an incident heat flux of 95 kW m$^{-2}$ and a nitrogen flow rate of 100 SLPM. Unlike PMMA, the measured products contained CO and $CO_2$ at levels significant enough to be included in the calculations. To obtain an accurate representation of the THC composition—rather than assuming it to be identical to the pyrolyzate, as was done for PMMA—the products of OSB pyrolysis were measured in the FPA. The measured CO and $CO_2$ yields were incorporated into the decomposition balance of OSB, written as:

$$\mathrm{CH_{2.2}O_{0.97}} \rightarrow \mu_{\mathrm{CO2}}\ \mathrm{CO_2} + \mu_{\mathrm{CO}}\ \mathrm{CO} + \mu_{\mathrm{C_pH_qO_r}}\ \mathrm{C_pH_qO_r} \quad (23)$$

In this expression, the μ terms represent the molar stoichiometric coefficients of each product species. $\mathrm{C_pH_qO_r}$ refers to a lumped hydrocarbon species whose elemental composition is determined from the pyrolysis product yields. The FID signal is used to quantify the amount of this hydrocarbon mixture released, as described in Section 2.5. The measured FID-based mass generation rate is denoted as $\dot{m}^t_{THC^*}$, which represents the uncorrected hydrocarbon mass generation rate before applying the OSB-specific calibration factor. In other words, $\dot{m}^t_{\mathrm{THC}^*}$ refers to the raw, uncorrected mass generation rate of the lumped species $C_pH_qO_r$, which is used in the reaction balance.

Analysis of the measured pyrolysis products from three pyrolysis experiments, showed that the ratio of the mass generation rate of gaseous products ($\dot{m}^t_i$, defined in Equation 7) to the transient mass-loss rate ($MLR^t$) evolved in two distinct regimes. During the early stage (approximately the first 30% of conversion), this ratio increased as OSB decomposition intensified. Beyond this point, the ratio reached a plateau, indicating a quasi-steady regime in which gasification and volatile release were relatively stable. This behavior is illustrated in Figure 7, which shows the ratio of the mass generation rate of $\mathrm{C_pH_qO_r}$, $\dot{m}^t_{\mathrm{THC}^*}$ (computed using Equation 7), prior to applying the FID correction factor to $MLR^t$ during pyrolysis. The shaded region represents ±2 standard errors.

Product yields were calculated using Equation 4 separately for the unsteady and quasi-steady phases of pyrolysis and are summarized in Table 6.

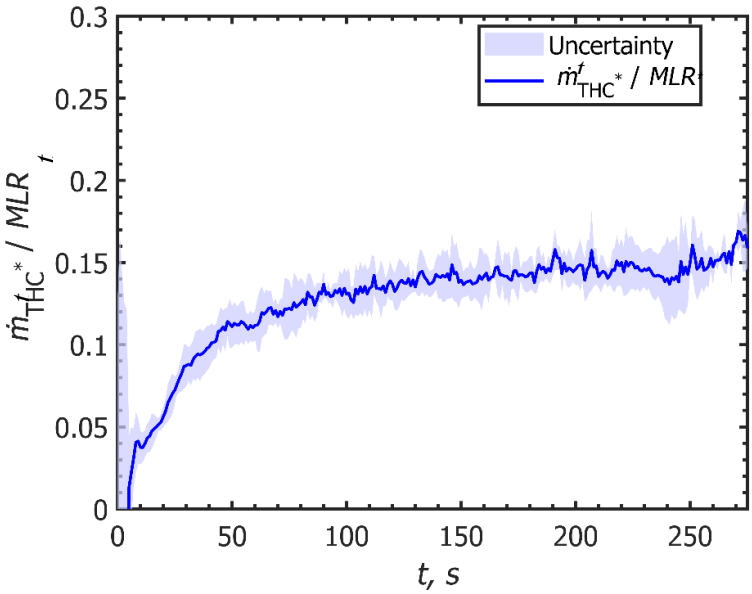


Figure 7. Average ratio of mass generation rate of lumped hydrocarbon species $C_pH_qO_r$, $\dot{m}^t_{\mathrm{THC}^*}$, to $MLR^t$ *from three OSB pyrolysis experiments*

Table 6. Species yields reported for two distinct phases of experiment

*Species yields (in mass per mass of pyrolyzed OSB) from three OSB pyrolysis experiments at 95 kW m$^{-2}$ and a100 SLPM $N_2$ flow rate. Yields for two distinct phases of experiment. Uncertainties represent ±2 standard errors*

| | **Unsteady phase (20-70 s)** | **quasi-steady phase (70-200 s)** |
|---|---|---|
| CO yield | 0.1085 ± 0.0025 | 0.1272 ± 0.0035 |
| $CO_2$ yield | 0.1117 ± 0.0029 | 0.1504 ± 0.0028 |
| THC yield * | 0.1005 ± 0.0032 | 0.1407 ± 0.0044 |

* *Yield based on the raw FID measurement, prior to applying the OSB-specific calibration factor.*

Only the quasi-steady-state yields (70–220 s), where the signals were stable, were used to determine the effective THC composition. Balancing Equation 23 using the yields from quasi-steady phase gave:

$$\mathrm{CH_{2.2}O_{0.97}} \rightarrow 0.1016\ \mathrm{CO_2} + 0.1350\ \mathrm{CO} + 0.7634\ \mathrm{CH_{2.882}O_{0.828}} \qquad 24$$

Therefore, THC composition would be $\mathrm{CH_{2.882}O_{0.828}}$. This derived THC formula is a more realistic representation of the gaseous hydrocarbons released during OSB combustion than simply assuming the pyrolyzate composition.

## 2.7 Calculations of heat release rate (*HRR*) and heat of combustion ($\Delta H_c^{eff}$)

In FPA (ASTM International, 2019), the time-resolved heat release rate per unit area, $HRRPUA^t$, is usually computed from the rates of generation of $CO_2$ and CO:

$$HRRPUA^t = \frac{1}{A_{samp}}\left(\Delta H_{\mathrm{CO2}}\dot{m}^t_{\mathrm{CO2},generated} + \Delta H_{\mathrm{CO}}\dot{m}^t_{\mathrm{CO},generated}\right) \quad 25$$

where $\Delta H_{\mathrm{CO2}}$ and $\Delta H_{\mathrm{CO}}$ are empirical constants that convert the mass generation rates to $HRRPUA^t$; and $A_{samp}$ is the initial surface area of the sample facing the heating lamps. This method for the calculation of $HRRPUA^t$ has a significant drawback with respect to a more widely used oxygen consumption calorimetry (Beyler, Croce, Dubay, Johnson, & McNamee, 2017; Biteau, et al., 2008). Unlike in the case of oxygen consumption calorimetry where the empirical constant that converts oxygen consumption to $HRRPUA^t$, $\Delta H_{\mathrm{O2}} = 13.1 \pm 0.6$ kJ $g_{O2}^{-1}$ is nearly independent of material composition (as long as the material is a hydrocarbon), $\Delta H_{\mathrm{CO2}}$ and $\Delta H_{\mathrm{CO}}$ vary significantly between different hydrocarbon fuels and additional calorimetric measurements are required to determine them for each material (Hurley, et al., 2016). Theoretically, it is possible to use the oxygen consumption calorimetry in an FPA because $\dot{m}^t_{\mathrm{O2},\,consumed}$ is computed from the test data. In practice, a high rate of dilution of the combustion effluent entering the duct with ambient air makes the difference in the measured $O_2$ volume fraction comparable with a drift in the analyzer baseline, which results in 7 ± 2% systematic error in the computed $HRRPUA^t$.

In this study, an attempt was made to address this drawback in the FPA $HRRPUA^t$ determination by designing a method that relies on $CO_2$ and CO generation data (which have a higher accuracy than oxygen consumption) but also uses the less fuel dependent empirical constant, $\Delta H_{\mathrm{O2}}$. In this method, once the combustion reaction of the pyrolyzate is balanced using the measured product yields, the stoichiometric coefficients of $O_2$ and $CO_2$ are used to calculate $\Delta H_{CO_2}$ from the known value of $\Delta H_{O_2}$ as:

$$\Delta H_{\mathrm{CO2}} = \frac{\mu_{\mathrm{O2}}\ MW_{\mathrm{O2}}\ \Delta H_{\mathrm{O2}}}{\mu_{\mathrm{CO2}}\ MW_{\mathrm{CO2}}} \quad 26$$

where $\mu_{O_2}$ and $\mu_{CO_2}$ are the stoichiometric coefficients of $O_2$ and $CO_2$ obtained from the balanced combustion equation. This constant depends on the composition of the gaseous pyrolyzate and the measured yields of the combustion products; therefore, it must be recalculated whenever changes in combustion conditions alter the product yields. The resulting value of $\Delta H_{CO_2}$ is used in Equation 25, with $\Delta H_{CO}$ set to zero, to compute the transient $HRRPUA^t$.

This method takes advantage of the time-resolved and highly-accurate $CO_2$ volume fraction measurement provided by the FPA. This method also takes into account the impact of the generation of incomplete combustion products on $HRRPUA^t$ and relies on a widely used oxygen consumption calorimetry principle. The effective heat of combustion of the gaseous pyrolyzate is computed from $HRRPUA^t$:

$$\Delta H_c^{eff} = \frac{A_{samp} \int_{t_1}^{t_2} HRRPUA^t dt}{\int_{t_1}^{t_2} MLR^t \, dt} \quad 27$$

where $t_1$ and $t_2$ correspond to times bounding the period of interest over which the effective heat of combustion is calculated. This method does not take into account that the $\Delta H_{O2}$ value varies somewhat with ventilation conditions. It is assumed that $\Delta H_{O2}$ is constant (13.1 ± 0.6 kJ $g_{O2}^{-1}$) because, even for the most under-ventilated conditions studied in this work, this variation remains within this constant's stated uncertainties.

The detailed procedure for balancing the combustion reaction and deriving the stoichiometric ratios for PMMA and OSB is presented in the following sections.

### 2.7.1 Poly(methyl Methacrylate) stoichiometric coefficient ratios calculation

The combustion reaction equation is balanced using the information on the atomic composition of the gaseous pyrolyzate and measured yields of $CO_2$, CO, THC, and PM. For PMMA, the following general reaction form was used:

$$\begin{aligned} &CH_{1.6}O_{0.4} + \mu_{O2}O_2 \\ &\rightarrow \mu_{CO2}CO_2 + \mu_{CO}CO + \mu_{PM}CH_{0.05}O_{0.06} + \mu_{THC}CH_{1.6}O_{0.4} + \mu_{H2O}H_2O \end{aligned} \quad 28$$

The PM formula in Equation 28 was obtained from elemental analysis of PM collected under both under-ventilated and well-ventilated conditions. Elemental content (C, H, N) was measured according to ASTM D5373 (ASTM International, 2016) oxygen was obtained by difference. Results are summarized in Table 7.

Table 7. Elemental analysis results of PM produced from PMMA combustion
*Under well- and under-ventilated conditions*

| **Component** | **ASTM test method** | **Mass fraction (% wt.), *GER* = 0.6** | **Mass fraction (% wt.), *GER*= 1.7** |
|---|---|---|---|
| Carbon | D 5373 | 89.94 | 95.61 |
| Hydrogen | D 5373 | 0.11 | 0.74 |
| Nitrogen | D 5373 | 0.37 | 0.30 |
| Oxygen | Calculated by difference | 9.58 | 3.35 |

From these analyses, PM compositions were converted from mass to mol fractions and normalized by the number of carbon moles. The resulting empirical formulas for well-ventilated and under-ventilated conditions were obtained as $CH_{0.01}O_{0.08}$ and $CH_{0.09}O_{0.03}$, respectively. The atomic compositions were found to be comparable, so the average value ($CH_{0.05}O_{0.06}$) was used in Equation 28.

To balance Equation 28 and determine the ratio $\frac{\mu_{O2}}{\mu_{CO2}}$ in Equation 26, the dimensionless parameters are defined as:

$$\alpha = \frac{\mu_{CO}}{\mu_{CO2}} = \frac{\text{Yield}_{CO}\, MW_{CO2}}{\text{Yield}_{CO2}\, MW_{CO}} \quad (29)$$

$$\beta = \frac{\mu_{PM}}{\mu_{CO2}} = \frac{\text{Yield}_{PM}\, MW_{CO2}}{\text{Yield}_{CO2}\, MW_{PM}} \quad (30)$$

$$\delta = \frac{\mu_{THC}}{\mu_{CO2}} = \frac{\text{Yield}_{THC}\, MW_{CO2}}{\text{Yield}_{CO2}\, MW_{THC}} \quad (31)$$

Balancing carbon gives:

$$\mu_{CO2} = \frac{1}{1 + \alpha + \beta + \delta} \quad (32)$$

Balancing hydrogen yields:

$$\mu_{H2O} = \frac{1}{2}(1.6 - 0.05\,\mu_{PM} - 1.6\,\mu_{THC}) = 0.8 - 0.025\,\beta\,\mu_{CO2} - 0.8\,\delta\,\mu_{CO2} \quad (33)$$

Balancing oxygen gives:

$$\mu_{O2} = 0.2 + \mu_{CO2} + 0.5\,\alpha\mu_{CO2} + 0.0125\,\beta\mu_{CO2} - 0.2\,\delta\,\mu_{CO2} \quad 34$$

Combining these relations leads to:

$$\frac{\mu_{O2}}{\mu_{CO2}} = 1.2 + 0.7\,\alpha + 0.2175\,\beta \quad 35$$

This ratio is then inserted into Equation 26 to compute $\Delta H_{CO_2}$, which is subsequently used for calculating both the transient $HRRPUA^t$ and $\Delta H_p$.

### 2.7.2 Oriented strand board stoichiometric coefficient ratios calculation

For OSB, the pyrolyzate is a multicomponent mixture consisting of $CO_2$, CO, and a lumped hydrocarbon species. Therefore, the species produced during pyrolysis (as given in Equatio 24) are treated as the reactants in the subsequent combustion balance. Accordingly, the combustion equation for OSB can be written in the following form:

$$0.1016\,CO_2 + 0.1350\,CO + 0.7634\,CH_{2.882}O_{0.828} + \mu_{O2}O_2 \rightarrow \mu_{CO2}CO_2 + \mu_{CO}CO + \mu_{PM}CH_{0.095}O_{0.04} + \mu_{THC}\,CH_{2.882}O_{0.828} + \mu_{H2O}\,H_2O \quad 36$$

The PM compositions from OSB combustions were also determined experimentally. Using the same elemental analysis procedure (ASTM D5373), the PM compositions were found to be $CH_{0.05}O_{0.04}$ for well-ventilated, and $CH_{0.14}O_{0.04}$ for under-ventilated conditions. Their average was used in the reaction balance. Results are shown in Table 8.

Table 8. Elemental analysis results of PM produced from OSB combustion
*Under well- and under-ventilated conditions*

| **Component** | **ASTM test method** | **Mass fraction (% wt.), *GER* = 0.5** | **Mass fraction (% wt.), *GER* = 1.1** |
|---|---|---|---|
| Carbon | D 5373 | 94.14 | 93.62 |
| Hydrogen | D 5373 | 0.41 | 1.09 |
| Nitrogen | D 5373 | 0.32 | 0.38 |
| Oxygen | Calculated by difference | 5.13 | 4.91 |

The definitions of $\alpha$, $\beta$, and $\delta$ from Equations 29 to 31 apply identically to OSB. Balancing the carbon atoms yields the same result as Equation 32.

By balancing the hydrogen atoms, the following expression is obtained:

$$\mu_{H2O} = \frac{1}{2}(2.2 - 0.095\,\mu_{PM} - 2.882\,\mu_{THC}) = 1.1 - 0.0475\,\beta\,\mu_{CO2} - 1.441\delta\,\mu_{CO2} \quad (37)$$

Similarly, by balancing the oxygen atoms:

$$\mu_{O2} = 0.0648 + \mu_{CO2} + 0.5\,\alpha\mu_{CO2} - 0.0038\beta\mu_{CO2} - 0.3065\delta\,\mu_{CO2} \quad (38)$$

Combining these relations gives:

$$\frac{\mu_{O2}}{\mu_{CO2}} = 1.0648 + 0.5648\alpha + 0.061\beta - 0.2417\delta \quad (39)$$

As in the PMMA case, this ratio is substituted into Equation 26 to determine $\Delta H_{CO_2}$ and subsequently calculate $HRRPUA^t$ and $\Delta H_c^{eff}$.

# 3 Material samples and test matrix

In this study, two common solid fuels relevant to fire scenarios were examined: PMMA and OSB, representing non-charring and charring fuels, respectively. Black cast PMMA samples were obtained from Evonik Industries and OSB samples from Home Depot (College Park, MD). The PMMA specimens had a diameter of 96 mm and a thickness of 6.1 mm, while the OSB samples had a diameter and thickness of 107 mm and 12 mm, respectively. As explained in the previous section, a larger OSB sample area was used to achieve higher $MLR^t$ values and thereby reach higher *GER*s within the limitations of the current air-flow adjustment system. The thickness of the insulation layer around the PMMA and OSB samples was 6.4 mm and 0.8 mm, respectively. The samples in the sample holder with the insulation layer are shown in Figure 8.

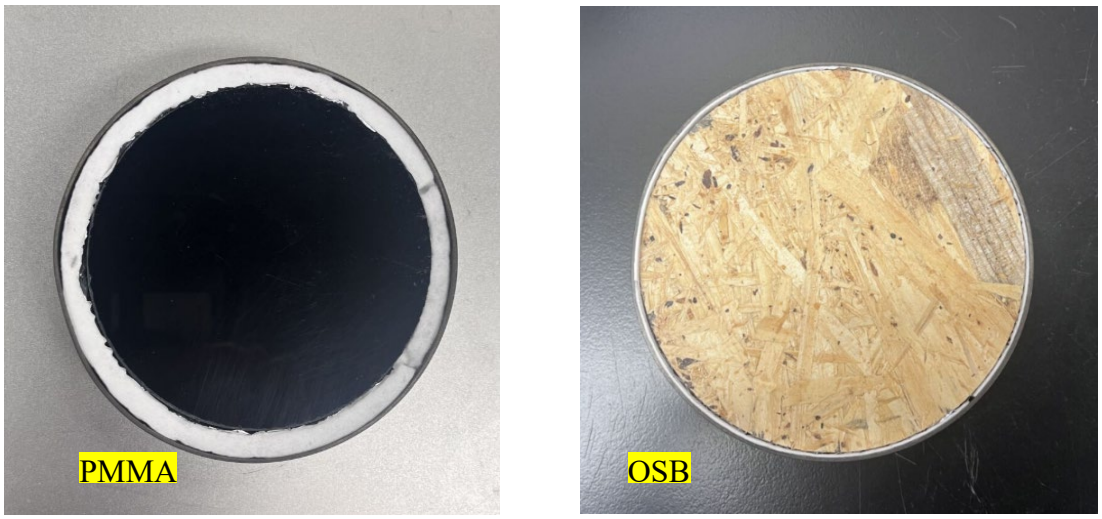


Figure 8. PMMA (96 mm diameter) and OSB (107 mm diameter) samples
*Samples were placed in the holder and wrapped in aluminum foil with an insulation layer*

Before testing, each PMMA sample was conditioned in a desiccator at 15% relative humidity and room temperature (20 – 23 °C) at least for 24 hours. The OSB samples were first oven-dried at 103 °C for 24 hours and then placed in the desiccator at 15% relative humidity for at least 24 hours prior to testing. The moisture content of the oven-dried OSB samples was measured as 5.74 ± 0.3%. The smoother surface of the OSB panel was oriented such that the incident heat flux was irradiating this surface.

For PMMA a total of 5 *GER* settings, 0.63, 1.10, 1.43, 1.69, and 1.96, were studied in this work, with every setting probed with five repeated tests. All these tests were performed at 75 kW $m^{-2}$ of set radiant heat flux. Additional tests were performed at 50 and 90 kW $m^{-2}$ radiant heat flux, and three *GER* values of 0.84 (50 kW $m^{-2}$), 1.54, and 1.92 (90 kW $m^{-2}$), with one test conducted for each combination of conditions. These runs were used to evaluate the predictive capability of the empirical model for species yields and $\Delta H_c^{eff}$, which was developed from the data collected at 75 kW $m^{-2}$, as discussed in a later section. In addition, three pyrolysis tests at 50 kW $m^{-2}$ heat flux and 100 SLPM $N_2$ flow rate were carried out to obtain the correction factor for FID-based THC measurements. PMMA test matrix is summarized in Table 9.

Table 9. PMMA test matrix

| **Test Type** | ***GER* Settings** | **Heat Flux (kW $m^{-2}$)** | **Air Flow / Notes** | **Number of Tests** |
|---|---|---|---|---|
| Constant-*GER* combustion tests | 0.63, 1.10, 1.43, 1.69, 1.96 | 75 | Calculated air flow for each *GER* | 5 repeats per *GER* (total 25 tests) |

| Test Type | *GER* Settings | Heat Flux (kW m$^{-2}$) | Air Flow / Notes | Number of Tests |
|---|---|---|---|---|
| Model-validation combustion tests[1] | 0.84, 1.54, 1.92 | 50, 90 | One test per combination | 3 tests |
| Pyrolysis tests | — (no $O_2$) | 50 | 100 SLPM $N_2$ | 3 tests |

[1] *GER* = 0.84 was tested at 50 kW m$^{-2}$; *GER* = 1.54 and 1.92 at 90 kW m$^{-2}$.

For OSB, three *GER* settings (0.50, 0.98, and 1.51) were studied at 95 kW m$^{-2}$, with each constant-*GER* experiment repeated five times. To further evaluate the empirical model developed from these data, three additional tests were carried out at 75 kW m$^{-2}$ under *GER* = 0.98. These tests also helped evaluate how different effective parameters influence species yields when the *GER* is held constant; these parameters are discussed in a later section. Finally, three pyrolysis experiments at 95 kW m$^{-2}$ heat flux and 100 SLPM $N_2$ flow rate were conducted to quantify the pyrolysis products and determine the FID correction factor for THC and to investigate the pyrolyzate composition change during the experiment. OSB test matrix is listed in Table 10.

Table 10. OSB test matrix

| Test Type | *GER* Settings | Heat Flux (kW m$^{-2}$) | Air Flow / Notes | Number of Tests |
|---|---|---|---|---|
| Constant-*GER* combustion tests | 0.5, 0.98, 1.51 | 95 | Calculated air flow for each *GER* | 5 repeats per *GER* (total 15 tests) |
| Combustion tests for model evaluation | 0.98 | 75 | Used to assess pyrolyzate composition | 3 tests |
| Pyrolysis tests | — (no $O_2$) | 95 | 100 SLPM $N_2$ | 3 tests |

# 4 Measurement results and model development

## 4.1 Poly(methyl Methacrylate) results

### 4.1.1 *Global equivalence ratio*

Figure 9 shows the *GER* data averaged over 10-second intervals observed in the constant-*GER* tests performed at 75 kW m$^{-2}$ of radiant heat flux. The 10-second resolution was chosen not only to match the air flow adjustment set points but also to exceed all sensor response times and a characteristic time, $t_{char}$, that the combusting mixture spends in the FPA test section, and thus ensure that the time resolution of all reported measurement results is not impacted by the instrumental limitations.

In Figure 9 dashed-line boxes mark the portions of tests for which species yields and $\Delta H_c^{eff}$ were computed. Error bars represent ± 2 standard errors. Discrete data points are linked using linear interpolation for visualization. *t* denotes the time after the drop of the shield. Each *GER* profile shown in Figure 9 is the mean computed from five repeated tests. Due to the fact that each mass flow controller set point time series was defined based on the $MLR^t$ data obtained in different, lower constant-*GER* tests, some variation in *GER* is observed with time even for the portions of the tests where *GER* control is imposed. To minimize the impact of this variation, only the portions of the tests where *GER* remained within ±10% of the mean were included in the species yield and $\Delta H_c^{eff}$ calculations. These time periods are marked in Figure 9 with dashed-line boxes. For the highest *GER* (*GER* = 1.96), only the final portion of the tests was used in the analysis because only in this final portion was the air flow rate high enough (> 75 SLPM) to prevent entrainment of the environmental air into the test section.

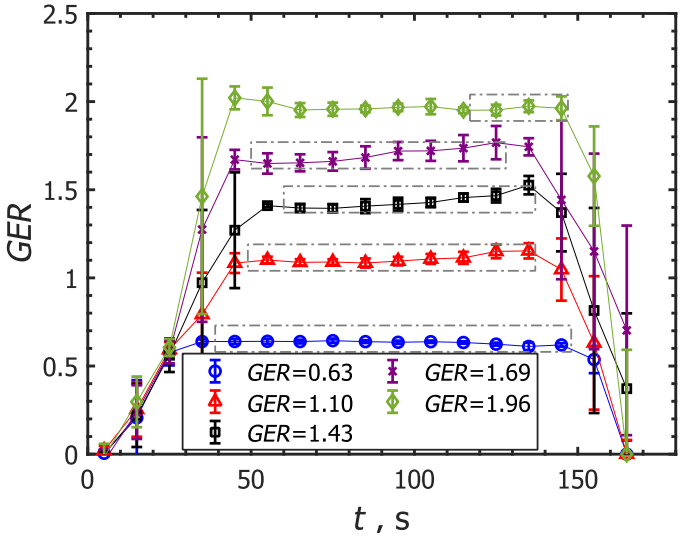


Figure 9. Mean *GER* obtained for tests performed on black cast PMMA

*At 75 kW m$^{-2}$ of set radiant heat flux*

### 4.1.2 Species yield and effective heat of combustion ($\Delta H_c^{eff}$)

The resulting species yield and $\Delta H_c^{eff}$ values are summarized in Table 11. The values exhibit expected trends: the $CO_2$ yields and $\Delta H_c^{eff}$ systematically decrease with increasing *GER*, while the yields of incomplete combustion products, CO, PM, and THC, systematically increase with increasing *GER*. The uncertainties are expressed as ± 2 standard errors computed from five repeated tests. To further validate the accuracy of these measurements, the ratio of the mass of carbon atoms in measured products to that in the corresponding amount of the pyrolyzate, referred to here as carbon balance (in percent), was computed for each *GER*:

$$\text{Carbon balance}_{\text{PMMA}}(\%) = 100\ \frac{m_{\text{CO2}}\ {MW_{\text{C}}}/{MW_{\text{CO2}}} + m_{\text{CO}}\ {MW_{\text{C}}}/{MW_{\text{CO}}} + m_{\text{PM}}\ {MW_{\text{C}}}/{MW_{\text{PM}}} + \ m_{\text{THC}}\ {MW_{\text{C}}}/{MW_{\text{THC}}}}{m_{\text{PMMA}}\ {MW_{\text{C}}}/{MW_{\text{PMMA}}}} \quad (40)$$

$$= 100\ \frac{0.2729\ m_{\text{CO2}} + 0.4288\ m_{\text{CO}} + 0.9224\ m_{\text{PM}} + 0.6\ m_{\text{THC}}}{0.6\ m_{\text{PMMA}}}$$

$$= 100\ (0.4548\ \text{Yield}_{\text{CO2}} + 0.7147\ \text{Yield}_{\text{CO}} + 1.5373\ \text{Yield}_{\text{PM}} + \ \text{Yield}_{\text{THC}}\ )$$

where m represents the mass of corresponding species, and $MW_{\text{C}}$ is the molecular weight of the carbon atom. The results of these calculations are provided in Table 11. These results indicate that the measured products account for close to 100% of carbon in the pyrolyzate. The fact that for highly under-ventilated conditions (*GER* > 1.5), the carbon balance is slightly above 100% is likely to be associated with the uncertainties that arise from the assumption that THC has the same atomic composition as the pyrolyzate.

Table 11. Species yields (mass per mass of pyrolyzate), carbon balance, $\Delta H_c^{eff}$

*Measured at constant-GER for PMMA*

| **GER** | **$CO_2$ Yield** | **CO Yield** | **PM Yield** | **THC Yield** | **NO Yield** | **HCN Yield** | **Carbon bal. %** | **$\Delta H_c^{eff}$, kJ g$^{-1}$** |
|---|---|---|---|---|---|---|---|---|
| 0.63 ± 0.01 | 2.041 ± 0.024 | (1.93 ± 0.36)×10$^{-2}$ | (1.45 ± 0.19)×10$^{-2}$ | (6.4 ± 1.6)×10$^{-3}$ | (3.3 ± 3.3)×10$^{-4}$ | (1.1 ± 1.1)×10$^{-20}$ | 97.01± 0.85 | 23.63 ±0.24 |
| 1.10 ± 0.01 | 1.741 ± 0.049 | (1.164± 0.071)×10$^{-1}$ | (2.80 ± 0.28)×10$^{-2}$ | (7.41 ± 0.93)×10$^{-2}$ | (8.5 ± 4.3)×10$^{-4}$ | (1.1 ± 1.1)×10$^{-20}$ | 99.2 ± 1.3 | 21.32 ± 0.51 |
| 1.43 ± 0.02 | 1.409 ± 0.058 | (1.855 ± 0.041)×10$^{-1}$ | (4.05 ± 0.25)×10$^{-2}$ | (1.793 ± 0.063)×10$^{-1}$ | (1.7 ± 0.9)×10$^{-3}$ | (3.0 ± 1.5)×10$^{-7}$ | 101.5 ± 2.7 | 18.33 ± 0.67 |
| 1.69 ± 0.05 | 1.232 ± 0.062 | (2.242 ± 0.044)×10$^{-1}$ | (4.20 ± 0.20)×10$^{-2}$ | (2.535 ± 0.011)×10$^{-1}$ | (3.0 ± 1.5)×10$^{-3}$ | (8.3 ± 4.2)×10$^{-7}$ | 103.8 ± 1.9 | 16.72 ± 0.68 |
| 1.96 ± 0.03 | 1.047 ± 0.034 | (2.625 ± 0.027)×10$^{-1}$ | (5.10 ± 0.26)×10$^{-2}$ | (3.011 ± 0.089)×10$^{-1}$ | (4.1 ± 2.0)×10$^{-3}$ | (8.3 ± 4.2)×10$^{-7}$ | 104.4 ± 1.2 | 15.07 ± 0.38 |

Some NO and HCN were detected in experiments, and their yields are reported in Table 11. The yields appear to increase with increasing *GER* – a trend that is consistent with those reported in

the literature (Hu, et al., 2018). Unfortunately, the concentrations of NO and HCN were near the sensitivity limits of the electrochemical sensors used in this study. Therefore, the uncertainties in these yields (calculated from the measured concentrations) are rather high, between ± 50 and ± 100% of the reported values.

Further analysis of species yields and $\Delta H_c^{eff}$ revealed that these data slowly and monotonically changed with time, even when *GER* is maintained at a constant value. The most significant changes were observed at higher *GER*. As an example, species yields obtained at *GER*=1.43 and $\Delta H_c^{eff}$ dependencies on time are shown in Figure 10 (a) and (b), respectively. It was hypothesized these changes are associated with the variation of the aforementioned characteristic time, $t_{char.}$, that the combusting mixture spends in the FPA test section.

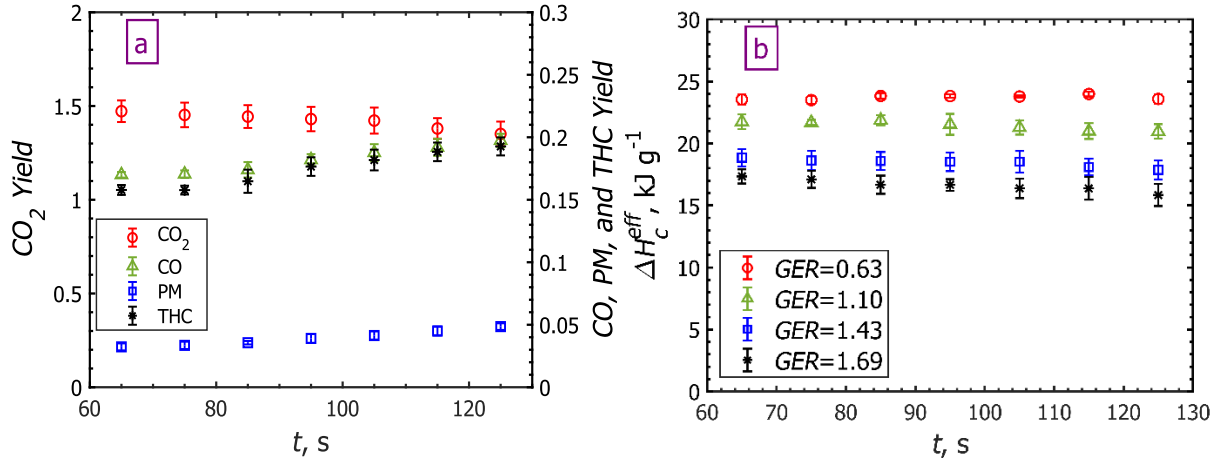


Figure 10. a) Species yield (mass per mass of pyrolyzate) at *GER*=1.43, b) $\Delta H_c^{eff}$ as function of time
*Only periods of constant-GER are shown. Error bars represent ± 2 standard errors for five repeated tests. t denotes time after drop of shield*

Based on the assumption of a plug flow, this characteristic time can be defined as:

$$t_{char} = \frac{V_{test\ section}\ MW_{air}\ P_{amb}}{(\dot{m}_{in}^{t} + MLR^{t})\ R\ T_{test\ section}^{t}} \qquad 41$$

where $V_{test\ section}$ is the volume of the test section where combustion takes place and combustion products reside before entering the exhaust system. This volume corresponds to the internal volume of the quartz tubes from the position of the sample to the top and is equal to 0.0163 m$^3$. $P_{amb}$ is the ambient pressure; and $T_{test\ section}^{t}$ is the average temperature of the gas mixture in the test section. Assuming no significant heat losses to the environment and no significant changes in the specific heat of the gas mixture, $T_{test\ section}^{t}$ can be estimated from the temperature and mass flow rate in the duct:

$$T^t_{test\ section} \approx \frac{T^t_{duct}\dot{m}^t_{duct} - T_{amb}(\dot{m}^t_{duct} - \dot{m}^t_{in} - MLR^t)}{\dot{m}^t_{in} + MLR^t} \quad (42)$$

where $T_{amb}$ is the ambient temperature. The data trends in Figure 10 (a) and (b) are consistent with an expectation that a reduction in $t_{char}$, which occurs in these tests as the air flow rate increases with time ($t$), promotes incomplete combustion and leads to an increase in the yields of incomplete combustion products and reduction in $\Delta H_c^{eff}$.

### 4.1.3 Empirical model development

A discrete nature of the species yields and $\Delta H_c^{eff}$ data and the dependence of this data on two independent variables, *GER* and $t_{char}$, dictates that an effective communication of this data can only be accomplished through a set of empirical expressions (a model) that interpolate the species yields data and relate the species yields and $\Delta H_c^{eff}$ to *GER* and $t_{char}$. The functional form of the empirical model for species yields was selected based on both physical reasoning and iterative testing of various mathematical expressions. The goal was to identify the simplest analytical expression that could accurately capture the observed trends in species yields with *GER* and $t_{char}$ and maintain the same monotonic trends outside of the data ranges that would also be consistent with the general understanding of the impact of *GER* and $t_{char}$ on the combustion process. Based on these considerations, the species yields were expressed as:

$$\text{Yield}_{i,model} = \frac{(t_{ref}/t_{char})^a}{1 + \exp\big(-b\ (GER - c)\big)} \quad (43)$$

This equation includes dimensionless adjustable parameters *a*, *b*, and *c* and a dimensional adjustable parameter, $t_{ref}$ (s). This equation was applied to species *i* including CO, PM, and THC. HCN and NO yields were not modeled because of their extremely small magnitudes and high uncertainties. The adjustable parameters were optimized for each species. The optimization consisted of scans of predefined ranges of all parameters (in small increments and in all possible combinations to minimize the mean absolute error between the model predictions and the corresponding experimental data. The values of the optimized parameters of PMMA species yield model (Equation 43) are summarized in Table 12.

Table 12. Optimized parameters for the PMMA species yield model

| Species | $t_{ref}$, s | $a$ | $b$ | $c$ |
|---|---|---|---|---|
| CO | 0.004 | 0.225 | 4.603 | 1.197 |
| PM | 0.065 | 0.881 | 3.194 | 1.176 |
| THC | 0.310 | 0.703 | 6.068 | 1.329 |

The $CO_2$ yield in the model was determined by enforcing carbon conservation, assuming a carbon balance equal to unity (i.e., 100% carbon recovery) in Equation 40.

Under this condition, the $CO_2$ yield model was calculated as follows:

$$\mathrm{Yield}_{\mathrm{CO2},model} = 2.199 - 1.571\,\mathrm{Yield}_{\mathrm{CO},model} - 3.380\,\mathrm{Yield}_{\mathrm{PM},model} - 2.199\,\mathrm{Yield}_{\mathrm{THC},model} \quad 44$$

The modeled heat of combustion of the gaseous pyrolyzate, $\Delta H_{c,model}^{eff}$, was determined from the modeled $CO_2$ yield:

$$\Delta H_{c,model}^{eff} = \mathrm{Yield}_{\mathrm{CO2},model}\,\Delta H_{\mathrm{CO2}} \quad 45$$

with $\Delta H_{\mathrm{CO2}}$ computed using Equation 26. The $\frac{\mu_{O2}}{\mu_{CO2}}$ ratio, described earlier and derived in Equations 29 to 35, was calculated using the modeled species yields.

A comprehensive comparison of the model predictions with the experimental data from which the model parameters were derived is provided in Figure 11. All $\Delta H_c^{eff}$ values reported in this figure were non-dimensionalized by dividing them by the heat of complete combustion of PMMA pyrolyzate $\Delta H_c^{comp} = 25.15$ kJ g$^{-1}$ determined from $\Delta H_{O2}$ and the stoichiometry of a complete combustion reaction. All experimental data were obtained at 75 kW m$^{-2}$ of set radiant heat flux.

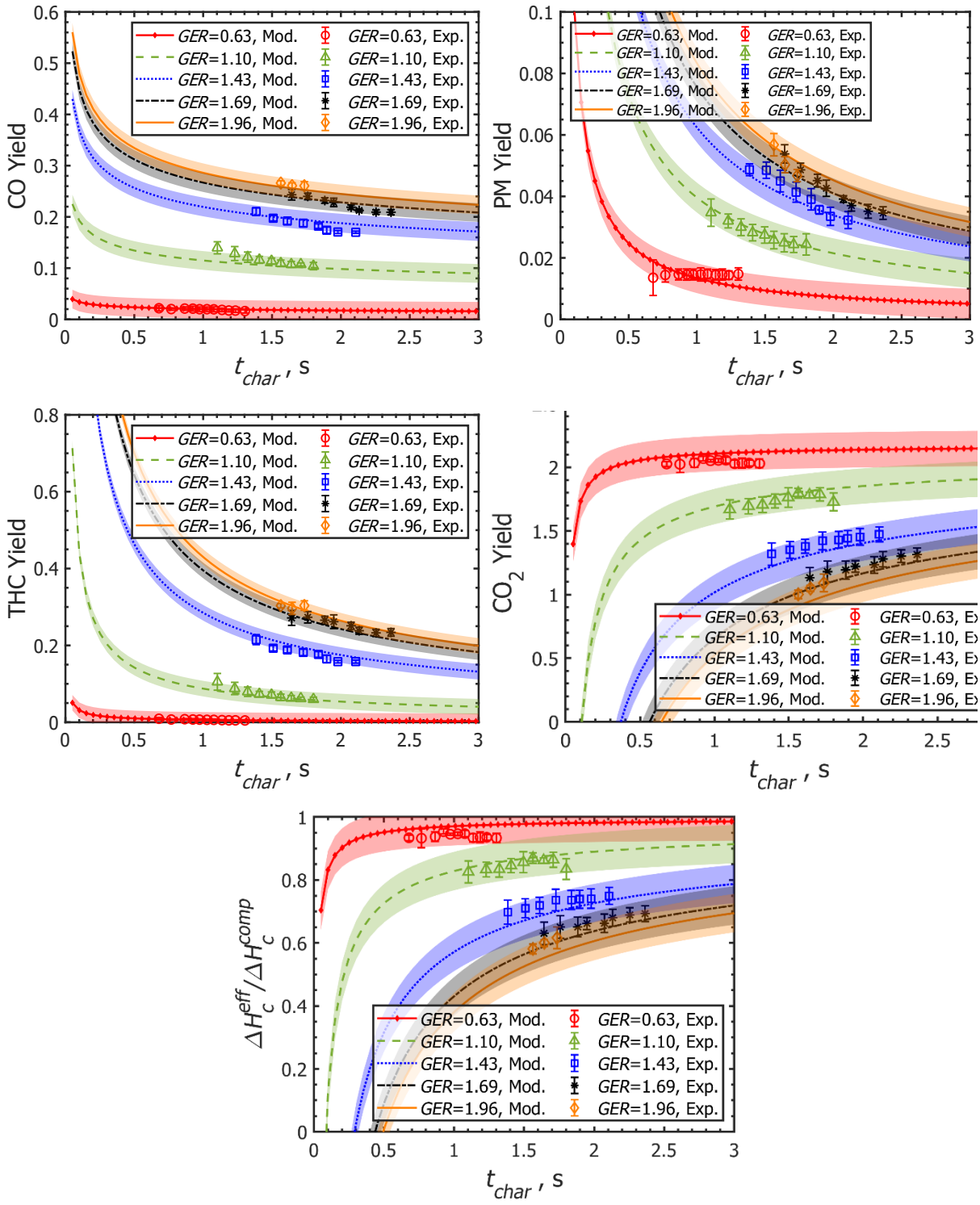


Figure 11. Comparison of experimental (Exp.) and modeled (Mod.) species yields (*Mass per mass of PMMA pyrolyzate*) and $\frac{\Delta H_c^{eff}}{\Delta H_c^{comp}}$

An examination of the data provided in Figure 11 led to a conclusion that the deviations between the model predictions and mean experimental data slightly exceed the uncertainties of the experimental data. Therefore, the uncertainties of the modeled quantities, including species yields and $\frac{\Delta H_c^{eff}}{\Delta H_c^{comp}}$, were defined as follows:

$$Modeled\ quantity\ uncertainty = \pm 2 \sqrt{\frac{1}{N_{exp}} \sum_{j=1}^{N_{exp}} \left(Exp.quantity_j - Mod.quantity_j\right)^2} \quad 46$$

where $N_{exp}$ represents the total number of experimental data points collected at all *GER* and $t_{char}$ values for a given modeled quantity. These uncertainties are shown in Figure 11 as shaded areas and also reported in Table 13. As Figure 11 indicates, these uncertainties include the overwhelming majority of the experimental data. In the figure, the error bars of experimental data represent experimental uncertainties expressed as ±2 standard errors.

Table 13. Uncertainties in modeled species yields and $\frac{\Delta H_c^{eff}}{\Delta H_c^{comp}}$ for PMMA.

| **Modeled quantity** | **Uncertainty** |
|---|---|
| $\text{Yield}_{\text{CO}}$ | ± 0.018 |
| $\text{Yield}_{\text{PM}}$ | ± 0.005 |
| $\text{Yield}_{\text{THC}}$ | ± 0.020 |
| $\text{Yield}_{\text{CO2}}$ | ± 0.139 |
| $\frac{\Delta H_c^{eff}}{\Delta H_c^{comp}}$ | ± 0.061 |

It's important to note that the $CO_2$ and $\frac{\Delta H_c^{eff}}{\Delta H_c^{comp}}$ models only work correctly when the characteristic time, $t_{char}$, is above a certain minimum value. When $t_{char}$ becomes too small, the model starts predicting values that are not physically meaningful (negative values), which cannot happen in reality. This cutoff occurs at $t_{char} \geq 0.657$ s. Therefore, the PMMA model should only be used for cases where $t_{char}$ is 0.657 seconds or higher.

### 4.1.4 Validation of the model

To further assess the accuracy of the developed model, its predictions were compared with the results of the constant-*GER* tests performed at 50 kW $m^{-2}$ and 90 kW $m^{-2}$, which were not used in the model parameterization. Figure 12 presents this comparison. The experimental data points do not include error bars because they are results of single tests performed at each explored *GER* setting. The overwhelming majority of the experimental data falls within the model's uncertainties, which indicates that the model is able to extrapolate to burning scenarios not used in the model parameterization.

### 4.1.5 Comparison of the model prediction with literature data

To further analyze the results obtained with the current methodology, the empirical model predictions were compared with the experimental data obtained for PMMA by Hull et al. (2000)using an SSTF. Since the time the combustion mixture spent inside the tube furnace ($t_{char}$) was not reported by Hull et al., it was estimated here from the information available in ISO-TS-19700 (2007) and Hull et al. (2000) to provide a more direct comparison with the current model. This comparison is shown in Figure 13 for all species yields which were reported by Hull et al. Most of the yields measured by Hull et al. are within the uncertainties of the current model. Hull et al. data uncertainties are not shown in the figure because the authors did not report them. The only significant discrepancy is in the PM yield at *GER* = 0.7. This discrepancy can be either due to the differences in the flame size in these two experiments or the differences in the PM measurement techniques. Hull et al. utilized a laser extinction method, whereas the current study employed a laser scattering method combined with gravimetric sampling. The error bars are model uncertainties computed using Equation 46.

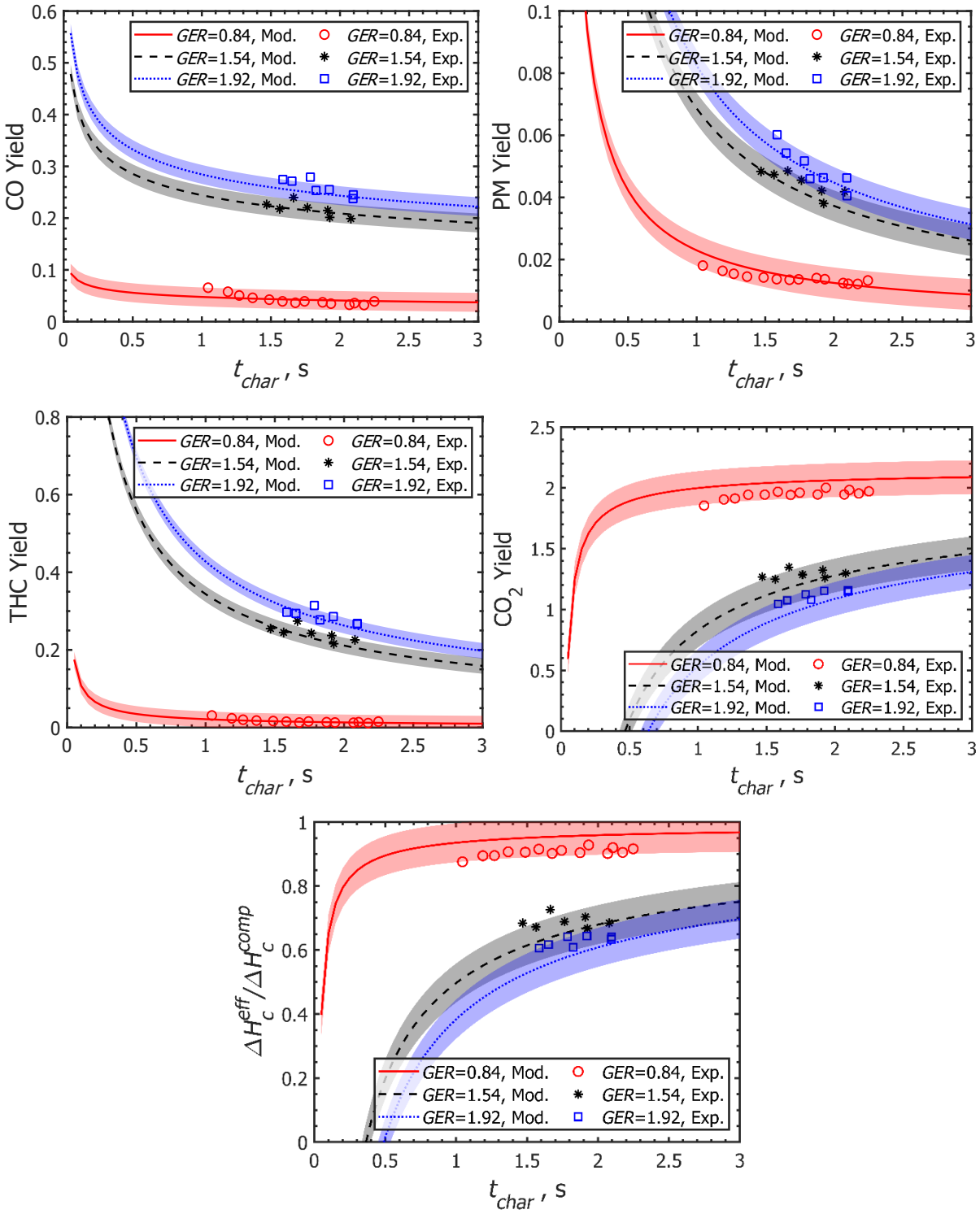


Figure 12. Comparison of experimental (Exp.) and modeled (Mod.) species yields (*In mass per mass of PMMA pyrolyzate*) and $\frac{\Delta H_c^{eff}}{\Delta H_c^{comp}}$

*Experimental data obtained at 50 kW m$^{-2}$ (GER = 0.84) and 90 kW m$^{-2}$ (GER = 1.54 and 1.92). Shaded areas model uncertainties computed using Eq. 46*

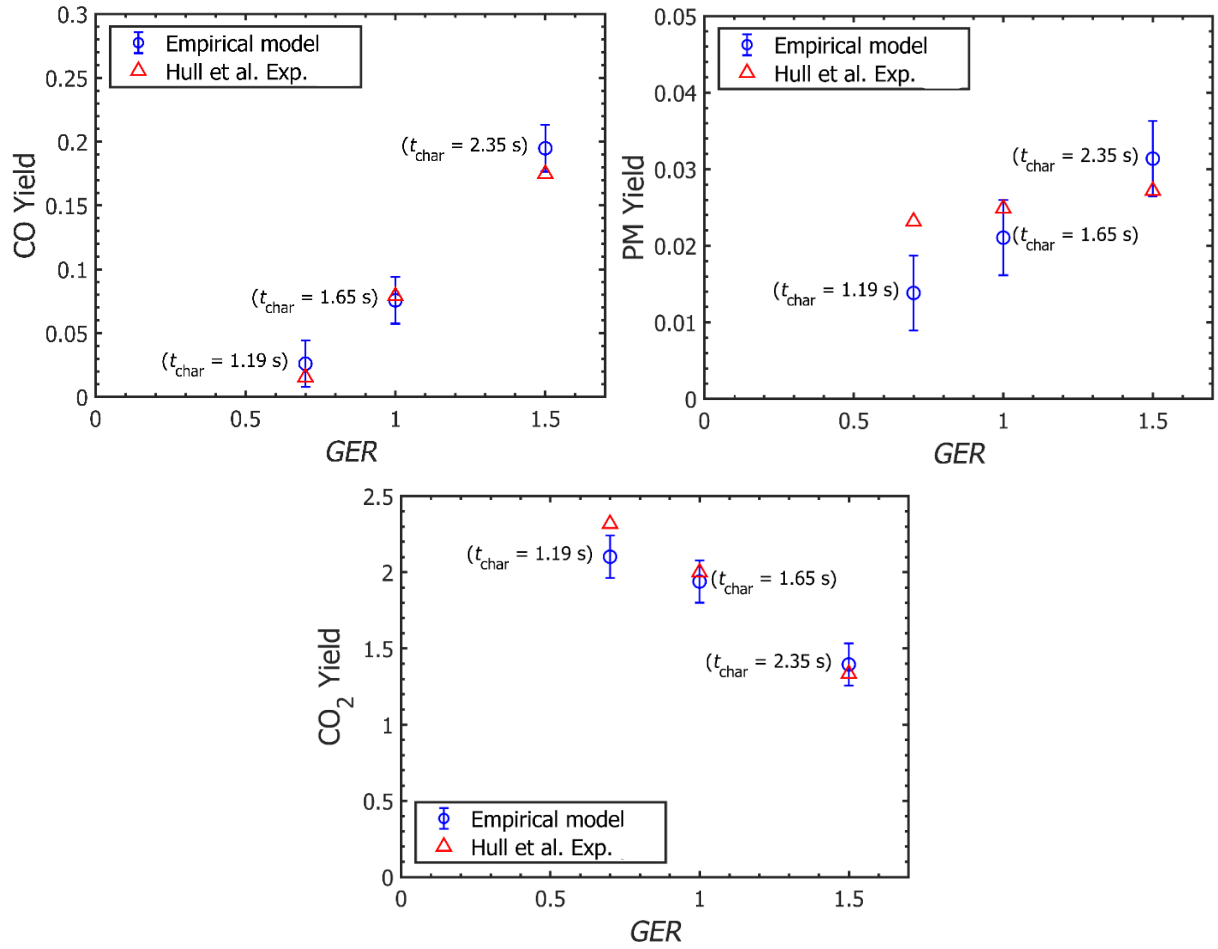


Figure 13. Comparison of species yields measured for PMMA using SSTF with current model predictions

Tewarson et al. (1993) also measured the yields of $CO_2$, CO, $O_2$, THC, and PM for PMMA in a wide range of *GER* using an FPA. Unfortunately, the authors did not report the information needed to compute $t_{char}$. Therefore, the yield calculations using the current model were performed by assuming $t_{char}$ = 1.78 s, obtained by averaging the characteristic times from tests conducted at 50 kW m$^{-2}$ and 90 kW m$^{-2}$ in the current study. A comparison between the current model and data from Tewarson et al. is provided in Figure 14. Uncertainties in the Tewarson et al. measurements, reported as ± 5%, are shown as error bars in the graphs.

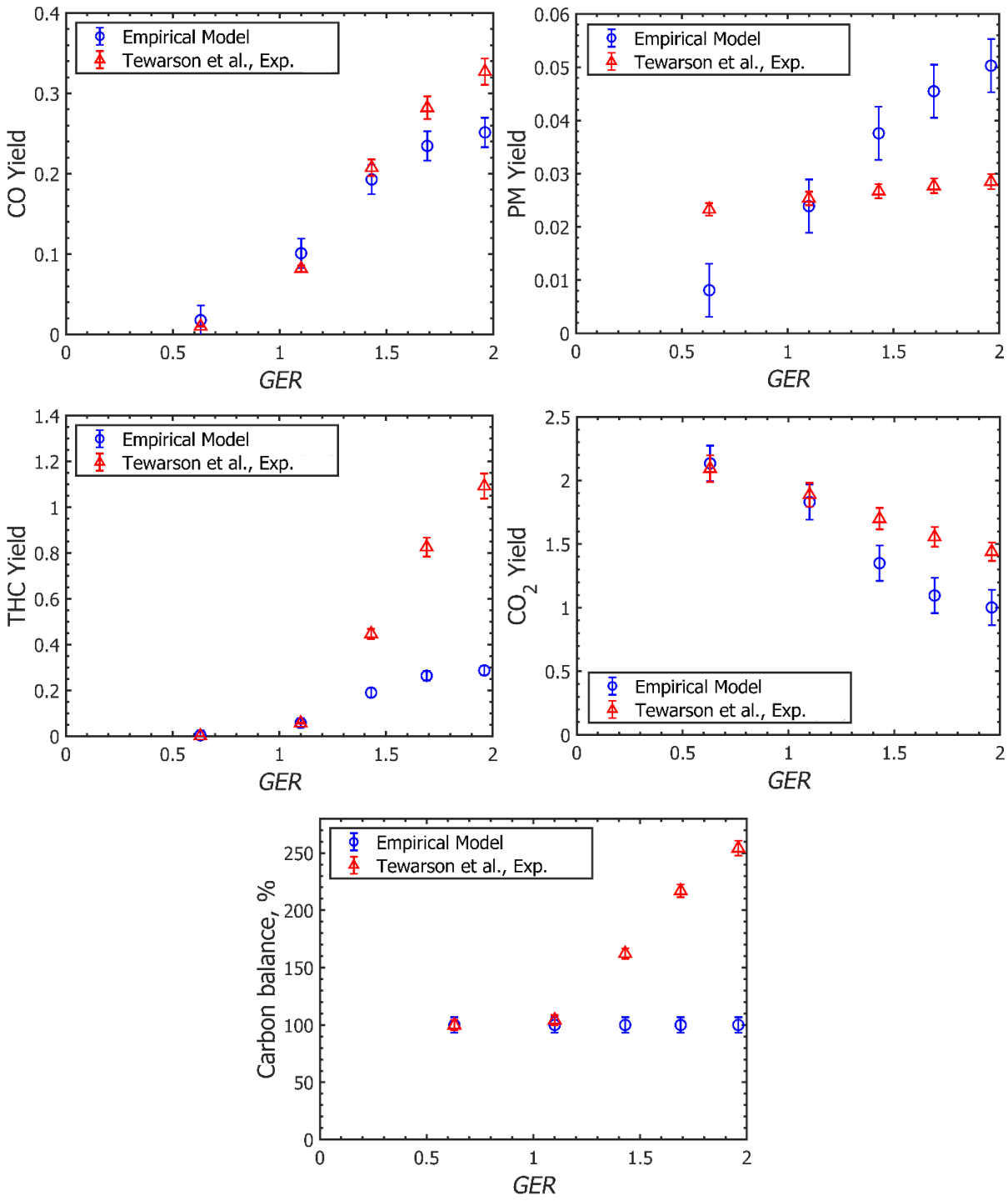


Figure 14. Comparison of species yields and carbon balance measured for PMMA using an FPA with current model

*Model predictions obtained at $t_{char}$ = 1.78 s. The error bars of the current data are model uncertainties computed using Eq. 25. The ± 5% uncertainties for experimental data are also shown on graphs*

At low *GER* (*GER* < 1.2), the Tewarson et al. species yields are in a reasonable agreement with the results of the current measurements. At high *GER* (*GER* > 1.4), significant discrepancies arise. The Tewarson et al. $CO_2$, CO, and THC yields become substantially higher than those computed using the current model, while Tewarson et al. PM yields become substantially lower. There are multiple factors that may have contributed to these discrepancies including non-constant-*GER* in Tewarson et al. tests and differences in the species measurement methodologies. The largest discrepancy is observed for THC. This discrepancy is also responsible for a rather large (up to 150%) overprediction of the carbon balance computed for the Tewarson et al. data and shown in Figure 14. One potential source of this discrepancy is associated with the manner in which Tewarson et al. report the data. The experimental results are reported as ratios of the yields divided by the corresponding well-ventilated yields. For THC, the well-ventilated yield is very small and thus potentially highly uncertain (far more uncertain than the reported uncertainty of ± 5% suggests), which may explain this major discrepancy.

### 4.1.6 Heat release rate per unit area ($HRRPUA^t$)

Here it is demonstrated that the developed model for PMMA combustion product yields and $\Delta H_c^{eff}$ can also be used to compute $HRRPUA^t$. The $HRRPUA^t$ was computed from the experimentally determined $\dot{m}^t_{\mathrm{CO2},generated}$ using Equation 25 with $\Delta H_{\mathrm{CO}}$ set to 0 and $\Delta H_{CO2}$ computed using Equation 26. The $\frac{\mu_{O2}}{\mu_{CO2}}$ ratio in Equation 26 was obtained from the modeled species yields using Equation 30. The modeled species yields were computed for each 10-second interval from the value of *GER* and $t_{char}$ associated with the interval. The $HRRPUA^t$ were calculated for all FPA experiments performed at 75 kW m$^{-2}$ set radiant heat flux including both constant- and variable-*GER* portions of these tests. The results of these calculations are presented in Figure 15. The uncertainties shown in this figure correspond to the uncertainties of the model which was assumed to be equal to that of $\frac{\Delta H_c^{eff}}{\Delta H_c^{comp}}$ values reported in Table 13. As the results shown in the figure indicate, increasing *GER* above 1.0 leads to an expected reduction in $HRRPUA^t$.

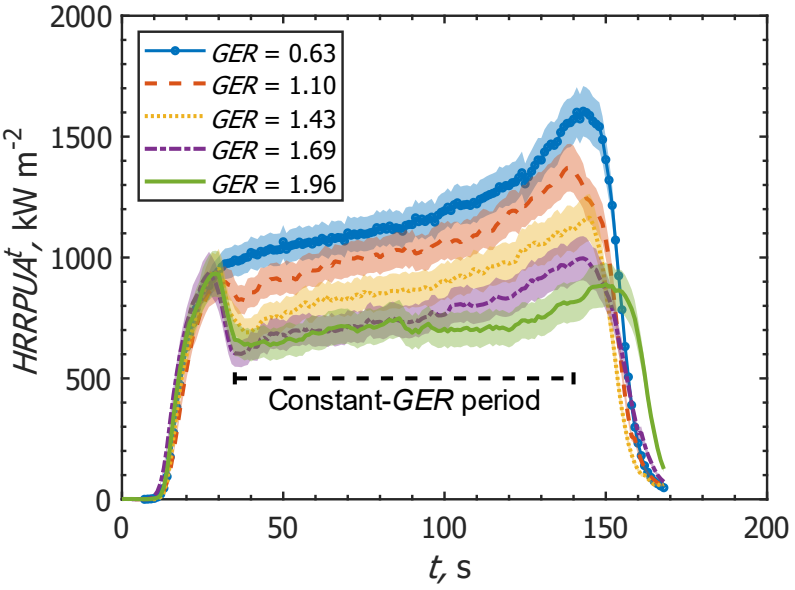


Figure 15. PMMA Heat release rates per unit area

*Computed for current FPA experiments performed at 75 kW m$^{-2}$ set radiant heat flux*

## 4.2 Oriented strand board results

### 4.2.1 *Global equivalence ratio*

Figure 16 shows the *GER* profiles from the OSB constant-*GER* experiments performed at 95 kW m$^{-2}$ radiant heat flux. The data are reported over 10-second intervals to smooth short-term fluctuations while still capturing changes on a timescale longer than the sensor response time and the characteristic time, $t_{char}$, of the gases in the FPA test section. The 10-second interval also matches the air flow adjustment set points.

In Figure 16, each curve represents the average of five repeated tests. Dashed-line boxes mark the portions of tests for which species yields and $\Delta H_c^{eff}$ were computed. Error bars represent ± 2 standard errors. Discrete data points are linked using linear interpolation for visualization. t denotes the time after the drop of the shield. Some variation in *GER* with time is evident, which arises from the way the air flow set points were determined using mass-loss data from preliminary experiments. To keep this variation from affecting the analysis, only the time periods where *GER* stayed within ±10% of the target value were used in calculating species yields and $\Delta H_c^{eff}$. These time periods are marked by dashed boxes in Figure 16.

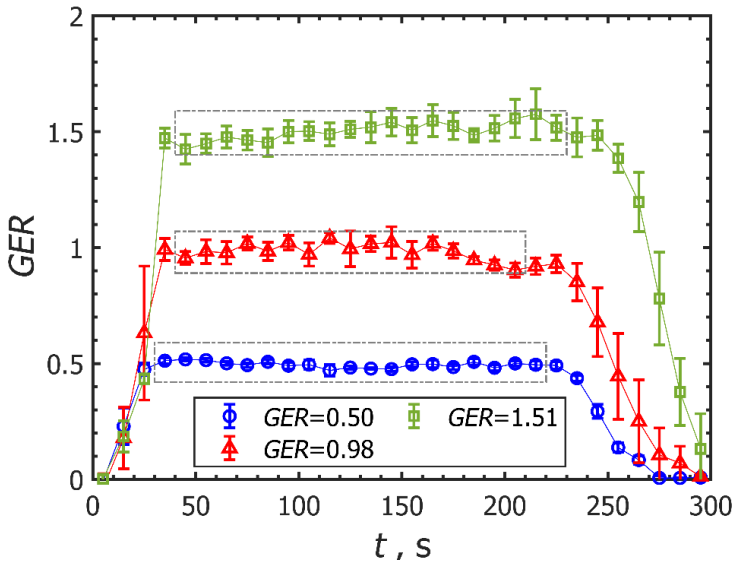


Figure 16. Mean *GER* obtained for tests performed on OSB at 95 kW m-2 set radiant heat flux

### 4.2.2 Species yield and heat of combustion ($\Delta H_c^{eff}$)

The species yields and $\Delta H_c^{eff}$ values obtained from the OSB tests are summarized in Table 14. Similar to PMMA, clear trends are observed: $CO_2$ yields and $\Delta H_c^{eff}$ decrease as *GER* increases, while the yields of CO, PM, and THC rise under more under-ventilated conditions. The uncertainties are expressed as ± 2 standard errors computed from five repeated tests. To assess the accuracy of these measurements, carbon balance calculations were performed by comparing the carbon measured in the products with the carbon content of the OSB pyrolyzate:

$$\text{Carbon balance}_{\text{OSB}}(\%) = 100\ \frac{m_{\text{CO2}}\ {MW_{\text{C}}}/{MW_{\text{CO2}}} + m_{\text{CO}}\ {MW_{\text{C}}}/{MW_{\text{CO}}} + m_{\text{PM}}\ {MW_{\text{C}}}/{MW_{\text{PM}}} + m_{\text{THC}}\ {MW_{\text{C}}}/{MW_{\text{THC}}}}{m_{\text{PMMA}}\ {MW_{\text{C}}}/{MW_{\text{PMMA}}}} \quad (47)$$

$$= 100\ \frac{0.2729\ m_{\text{CO2}} + 0.4288\ m_{\text{CO}} + 0.942\ m_{\text{PM}} + 0.427\ m_{\text{THC}}}{0.404\ m_{\text{OSB}}}$$

$$= 100\ (0.676\ \text{Yield}_{\text{CO2}} + 1.061\ \text{Yield}_{\text{CO}} + 2.332\ \text{Yield}_{\text{PM}} + 1.057\ \text{Yield}_{\text{THC}})$$

The balances, listed in Table 14, are close to 100% for all conditions, indicating that the major carbon-containing products were effectively captured. At high *GER* values, the carbon balance slightly exceeded 100%, which is likely associated with uncertainties in the assumed THC elemental composition. The overestimation (up to 107.7%) mainly reflects the sensitivity of the carbon balance to the assumed elemental composition of THC. Several chemically reasonable THC compositions can yield a near-perfect carbon balance. For instance, when a representative compound such as formic acid ($CH_2O_2$) is used as the THC composition, the carbon balance

remains within 100% ± 3% across all ventilation conditions. At *GER* = 1.51, this THC composition results in a carbon balance of 100.3%. This indicates that the observed deviation at high *GER* likely stems from the chosen THC formulation rather than from measurement errors.

The measured NO yields were low, on the order of $10^{-4}$, and increased slightly with *GER*. Although a modest upward trend is observed, the difference between *GER* = 1.0 and 1.5 is within experimental uncertainty and therefore not considered significant. The HCN yields were near zero for all ventilation conditions, with a measurable value of only $(2.0 \pm 2.0) \times 10^{-7}$at *GER* = 1.51. It should also be noted that the concentrations of NO and HCN were close to the detection limits of the electrochemical sensors used, resulting in high uncertainty—estimated at ±100% of the reported values.

Table 14. Species yields, carbon balance, effective heats of combustion of pyrolyzate ($\Delta H_c^{eff}$)
*Measured at constant-GER for OSB*

| ***GER*** | **$CO_2$ Yield** | **CO Yield** | **PM Yield** | **THC Yield** | **NO Yield** | **HCN Yield** | **Carbon bal. %** | **$\Delta H_c^{eff}$, kJ g$^{-1}$** |
|---|---|---|---|---|---|---|---|---|
| 0.50 ± 0.01 | 1.394 ± 0.009 | (4.39 ± 0.30)×10$^{-3}$ | (1.69 ± 0.06)×10$^{-2}$ | (3.50 ± 0.34)×10$^{-3}$ | (1.15 ± 1.15)×10$^{-4}$ | 0 | 98.96± 0.71 | 14.20 ±0.10 |
| 0.98 ± 0.01 | 1.284 ± 0.012 | (3.133± 0.162)×10$^{-2}$ | (2.027 ± 0.076)×10$^{-2}$ | (3.468 ± 0.194)×10$^{-2}$ | (7.2 ± 7.2)×10$^{-4}$ | 0 | 98.46 ±0.66 | 13.21 ± 0.11 |
| 1.51 ± 0.02 | 1.026 ± 0.012 | (1.207 ± 0.056)×10$^{-1}$ | (2.792 ± 0.151)×10$^{-2}$ | (1.809 ± 0.137)×10$^{-1}$ | (7.52 ± 7.52)×10$^{-4}$ | (2.01 ± 2.01)×10$^{-7}$ | 107.70 ±2.7 | 10.83 ± 0.14 |

Analysis of the species yield trends over time for OSB, shown for one *GER* condition in Figure 17, suggests that factors beyond *GER* and characteristic time may influence the observed trend. For PMMA, the yield–time curves showed a smooth, monotonic drift that could be directly attributed to changes in $t_{char}$, consistent with PMMA's constant pyrolyzate composition assumption. In contrast, the OSB data exhibits a more complex evolution: the trends are less uniform and lack the well-defined dependence observed for PMMA (Figure 10). This behavior is likely related to the fact that OSB pyrolyzate composition changes as the underlying wood constituents decompose in stages. Because such compositional shifts can potentially affect species yields and the effective heat of combustion, the next section examines how the OSB pyrolyzate composition evolves over time and whether these variations meaningfully influence the species yields and the effective heat of combustion.

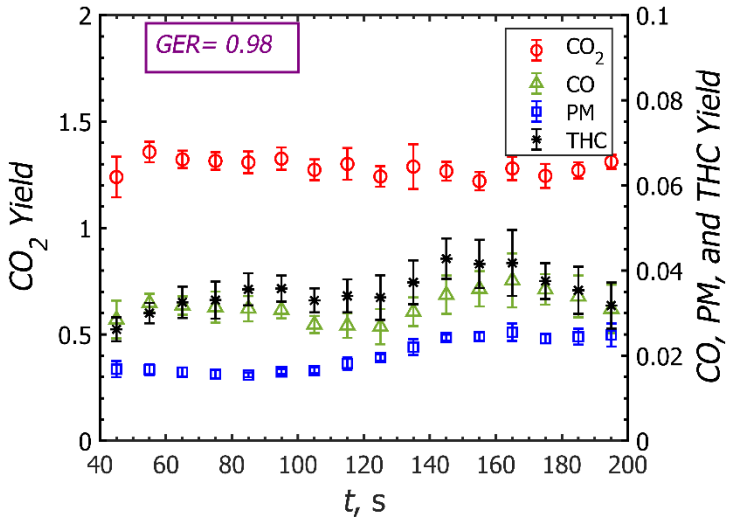


Figure 17. Species yield at *GER*=0.98
*Only period of constant-GER is shown;*
*error bars represent ± 2 standard errors for five repeated tests, t denotes time after drop of shield.*

### 4.2.3 Investigating the change of composition of pyrolyzate

Because the wood polymer matrix undergoes staged thermal degradation (Shafizadeh, 1982), the composition of the pyrolyzate is expected to evolve throughout an OSB experiment in the FPA. These variations in pyrolyzate composition may influence the formation of combustion products. Therefore, in addition to *GER* and characteristic time, it is necessary to examine whether pyrolyzate composition acts as a meaningful controlling parameter.

To investigate this effect, OSB pyrolysis tests were conducted under an external heat flux of 95 kW $m^{-2}$ with a nitrogen flow of 100 SLPM. The major pyrolysis products—including CO, $CO_2$, and THC—were measured. Since the instantaneous composition of the pyrolyzate cannot be directly identified during burning, a progress variable must be introduced that correlates with expected shifts in the volatile mixture due to the staged degradation of wood components.

For this purpose, the degree of decomposition, $DoD^t$, was defined as the ratio of the cumulative mass pyrolyzed up to time $t$ to the total mass pyrolyzed during the entire test:

$$DoD^t = \frac{\int_0^t MLR^t \, dt}{\int_0^{t_{end}} MLR^t \, dt} \tag{48}$$

where $t_{end}$ is the time corresponding to the end of flaming or the termination of pyrolysis, defined as the point at which product generation ceases and no gas is released. In the pyrolysis

experiments, the FID signal was recorded and the corresponding uncorrected mass generation rate, $\dot{m}^t_{\mathrm{THC}^*}$, was calculated from it using Equation 7, prior to applying the OSB-specific calibration factor. The ratio $\frac{\dot{m}^t_{\mathrm{THC}^*}}{MLR^t}$ was then used as a rough indicator of the relative hydrocarbon contribution to the total pyrolyzate at time $t$.

Thus, $DoD^t$ describes the extent of thermal decomposition in the solid, whereas the ratio $\frac{\dot{m}^t_{\mathrm{THC}^*}}{MLR^t}$ characterizes the instantaneous composition of the released vapors. Although $DoD^t$ does not uniquely determine the pyrolyzate composition, it provides a monotonic progress variable that is expected to correlate with shifts in the volatile mixture arising from staged wood degradation.

Comparing these two quantities enables us to assess whether the evolution of the volatile mixture can be parameterized using $DoD^t$ alone, or whether additional factors—such as characteristic time and ventilation—exert stronger control over the observed combustion-product yields. The relationship between $\frac{\dot{m}^t_{\mathrm{THC}^*}}{MLR^t}$ and $DoD^t$ is shown in Figure 18, which provides the dependence of the pyrolyzate composition metric ($\frac{\dot{m}^t_{\mathrm{THC}^*}}{MLR^t}$) on the degree of decomposition in a pyrolysis test.

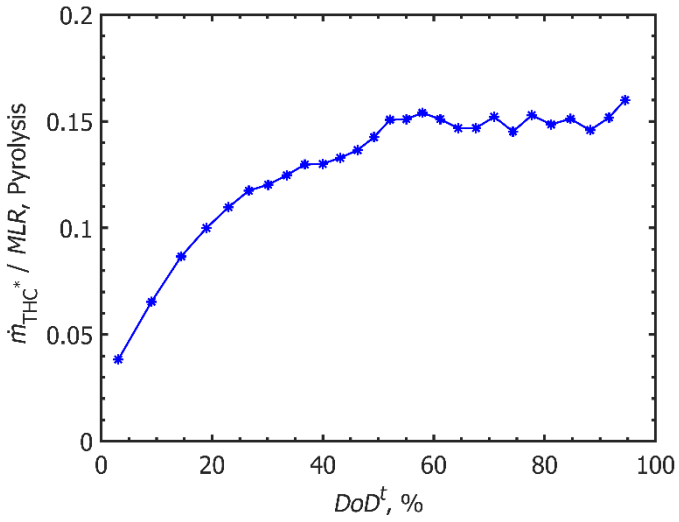


Figure 18. Dependence of pyrolyzate composition metric ($\frac{\dot{m}^t_{THC^*}}{MLR^t}$) on degree of decomposition *In a pyrolysis experiment at 95 kW m$^{-2}$ and 100 SLPM $N_2$ flow rate*

For the combustion experiments conducted at constant-*GER*, the degree of decomposition $DoD^t$ was calculated from the measured mass-loss histories. Species yields from the combustion tests were then mapped to the corresponding values of $DoD^t$. This allowed direct comparison between the gas-phase pyrolyzate composition indicator from pyrolysis, $\frac{\dot{m}^t_{\mathrm{THC}^*}}{MLR^t}$, and the species yields from combustion, both evaluated at the same degree of decomposition.

If pyrolyzate composition is a dominant controlling parameter, then combustion yields at a given $DoD^t$ should exhibit a clear, consistent relationship with the pyrolyzate composition indicator. In other words, for different *GER*s and species, points corresponding to the same $DoD^t$ would be expected to align or follow a similar trend when plotted against $\frac{\dot{m}^t_{\mathrm{THC}^*}}{MLR^t}$. Figure 19 presents this comparison. The results show that a consistent correspondence between the composition metric and the combustion yields does not exist across *GER*s. Although the ratio $\frac{\dot{m}^t_{\mathrm{THC}^*}}{MLR^t}$ clearly varies with $DoD^t$ (Figure 18), these variations do not translate into predictable changes in the combustion-product yields. For example, at the same degree of decomposition, the change of yields of CO, $CO_2$, and THC with pyrolyzate composition metric often differ substantially across ventilation conditions.

The observed inconsistent trends in Figure 19 indicate that while the pyrolyzate composition does evolve during decomposition, its influence on combustion-product formation is secondary. Ventilation and the associated characteristic time exert a stronger influence on combustion products yields. Therefore, although $DoD^t$ provides a useful measure of solid-phase reaction progress and correlates with changes in pyrolyzate composition, it does not serve as a reliable organizing parameter for predicting species yields. Instead, characteristic time, together with *GER*, emerges as the primary factor controlling the formation of CO, $CO_2$, and unburned hydrocarbons.

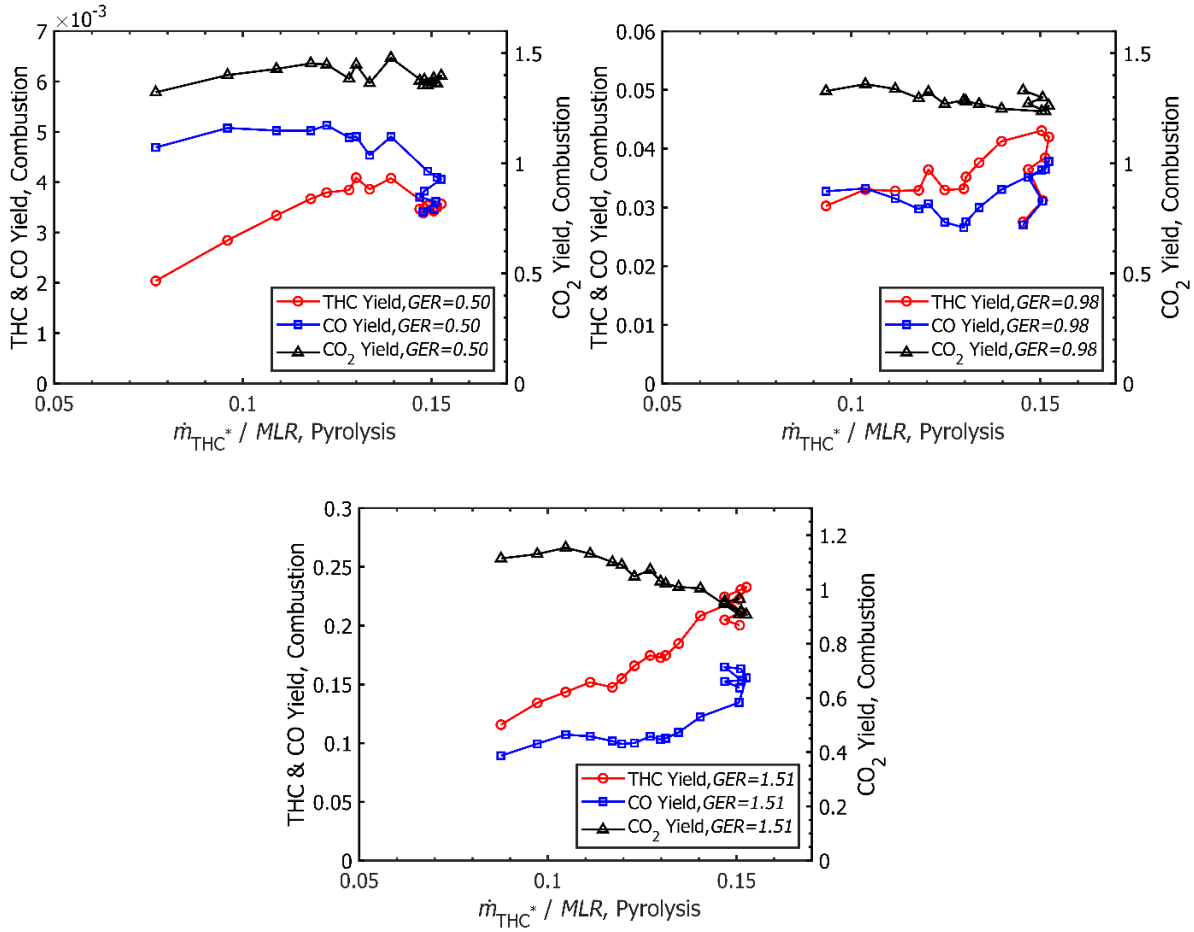


Figure 19. Trend of combustion species yields plotted against pyrolyzate composition metric $\frac{\dot{m}^{t}_{\mathrm{THC}^*}}{MLR^{t}}$

*Both evaluated at same degree of decomposition*

To further assess whether pyrolyzate composition can explain variations in combustion-product yields, an additional set of OSB experiments was performed at the same ventilation condition (*GER* = 0.98) but under a different external heat flux (75 kW m$^{-2}$). Lowering the heat flux increased the characteristic time of the combustion mixture in the test section while still allowing overlap in the range of achievable $t_{char}$ values. As a result, this test matrix provides pairs of data with the same *GER*, similar degrees of decomposition, but different characteristic times. The OSB experiments at 75 kW m$^{-2}$ repeated three times.

If pyrolyzate composition governed the formation of combustion products, then species yields at the same $DoD^{t}$ would be expected to agree even when $t_{char}$ differs.

To test this hypothesis, two types of comparisons were performed:

1. Matching $DoD^t$ between the 95 kW m$^{-2}$ and 75 kW m$^{-2}$ tests (different $t_{char}$)
2. Matching $\mathrm{t_{char}}$ between the two tests (allowing $DoD^t$ to differ)

The relative difference between yields from the two heat-flux conditions was quantified using:

$$Difference(\%) = mean\left(\frac{|\ \mathrm{Yield}_{i,95} - \mathrm{Yield}_{i,75}\ |}{\mathrm{Yield}_{i,95}}\right) \times 100 \qquad 49$$

where $\mathrm{Yield}_{i,95}$ and $\mathrm{Yield}_{i,75}$ are the yields of species *i* at heat flux of 95 kW m$^{-2}$ and 75 kW m$^{-2}$. When species yields were compared at the same degree of decomposition, the differences between the two heat-flux conditions were relatively large compared to the difference between the yields at the same characteristic time. This means that combustion yields from the 75 kW m$^{-2}$ and 95 kW m$^{-2}$ tests collapse more closely when plotted as a function of $t_{char}$ than when plotted as a function of $DoD^t$. These comparisons are illustrated in Figure 20, and the numerical differences (Equation 49) in percent are summarized in Table 15.

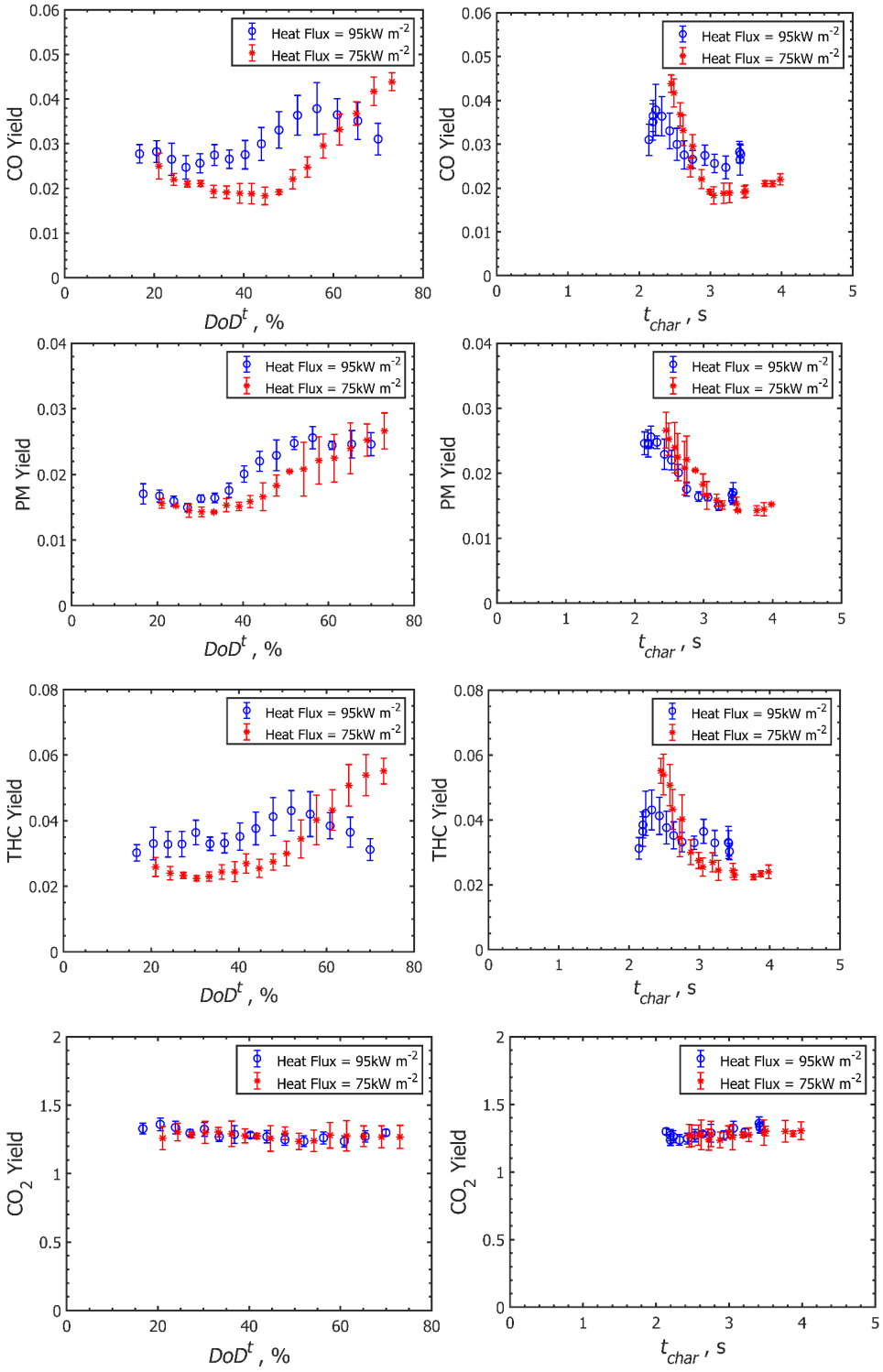


Figure 20. Comparison of species yields plotted against $DoD^t$ and $t_{char}$ for OSB combustion *Tests performed at 75 kW·m⁻² and 95 kW·m⁻² under fixed GER of 0.98. Uncertainties represent ±2 standard errors.*

Table 15. Relative differences between species yields
*Measured at 75 kW m$^{-2}$ and 95 kW m$^{-2}$ under GER = 0.98*
*When organized by degree of decomposition and by characteristic time*

| | **CO** | **PM** | **THC** | **$CO_2$** |
|---|---|---|---|---|
| Yield differences at matched $t_{char}$, % | 26.77 | 10.87 | 24.86 | 2.91 |
| Yield differences at matched $DoD^t$, % | 30.89 | 16.91 | 31.57 | 2.69 |

This behavior demonstrates that characteristic time is a more robust influencing parameter than the degree of decomposition for organizing and extrapolating species yield. Although $DoD^t$ is a useful progress variable that reflects the advancement of solid-phase decomposition and correlates with changes in the volatile mixture, matching $DoD^t$ is not sufficient to predict combustion-product formation. Instead, comparison at constant $t_{char}$ shows that residence-time-controlled oxidation processes exert a stronger influence on the formation of CO, $CO_2$, and THC.

Consequently, characteristic time, together with *GER*, is adopted as a primary controlling parameter, while the influence of pyrolyzate composition alone is considered secondary.

### 4.2.4 Empirical model development

For OSB, the same general approach used for the case of PMMA was used to develop an empirical model for species yields. The model structure was chosen after considering both physical reasoning, with the aim of identifying the simplest expression that could reproduce the observed dependence of species yields on *GER* and $t_{char}$. It was also important that the model preserve the expected monotonic behavior outside the experimental data range and remain consistent with the general understanding of how *GER* and $t_{char}$ influence combustion. On this basis, the yields were described the same as the Equation 43 with the constant values as in Table 16:

Table 16. Optimized parameters for OSB species yield model (Eq. 43).

| **Species** | $t_{ref}$, **s** | ***a*** | ***b*** | ***c*** |
|---|---|---|---|---|
| CO | 0.210 | 0.720 | 4.790 | 1.313 |
| PM | 0.221 | 1.192 | 1.542 | 1.277 |
| THC | 0.615 | 0.950 | 5.530 | 1.339 |

This formulation was applied to CO, PM, and THC, while HCN and NO were excluded because of their very low yields and high associated uncertainties. The adjustable parameters were optimized separately for each species by scanning predefined ranges for all variables in small

increments and testing all possible parameter combinations. The goal was to minimize the mean absolute error between model predictions and the experimental results.

The $CO_2$ yield was computed in the model by imposing carbon conservation in Equation 47:

$$\text{Yield}_{\text{CO2},model} = 1.480 - 1.571\ \text{Yield}_{\text{CO},model} - 3.452\ \text{Yield}_{\text{PM},model} - 1.563\ \text{Yield}_{\text{THC},model} \quad (50)$$

The modeled heat of combustion of the gaseous pyrolyzate, $\Delta H_{c,model}^{eff}$, was determined from the modeled $CO_2$ yield using Equation 45, following the same procedure described for PMMA. For OSB, the $\frac{\mu_{O2}}{\mu_{CO2}}$ ratio was calculated from Equation 39 based on the modeled species yields.

A comprehensive comparison of the model predictions with the experimental data from which the model parameters were derived is provided in Figure 21. Experimental data were obtained at 95 kW $m^{-2}$ of set radiant heat flux. All $\Delta H_c^{eff}$ values reported in this figure were non-dimensionalized by dividing them by the heat of complete combustion of OSB pyrolyzate $\Delta H_c^{comp} = 15.01$ kJ $g^{-1}$ determined from the stoichiometry of a complete combustion reaction. In this Figure, the error bars represent experimental uncertainties expressed as two standard errors. Shaded areas are model uncertainties computed using Equation 46.

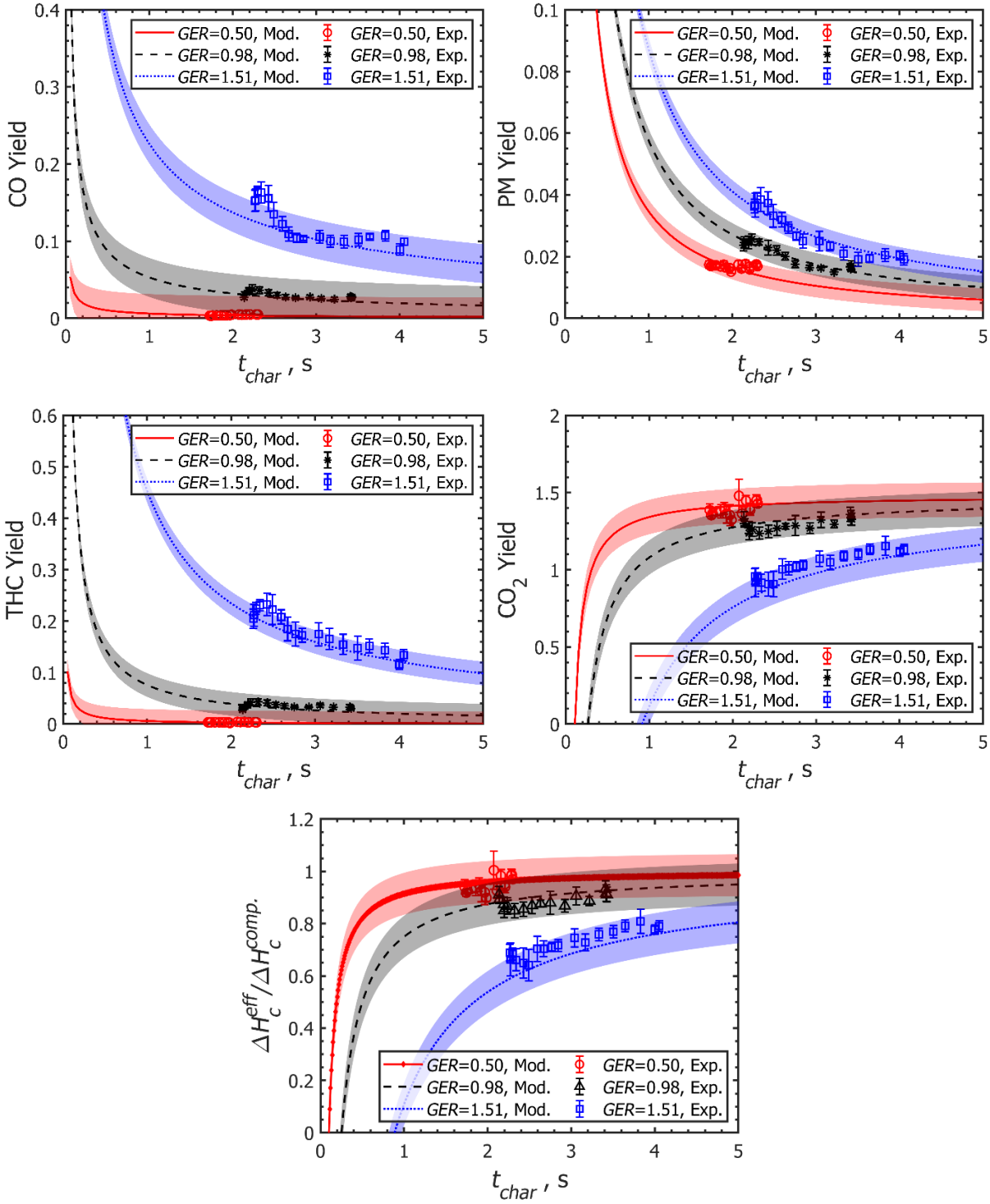


Figure 21. Comparison of experimental and modeled species yields (*Mass per mass of OSB pyrolyzate*) and $\frac{\Delta H_c^{eff}}{\Delta H_c^{comp}}$

Analysis of the OSB data (Figure 21) showed that the differences between the model predictions and the mean experimental values were slightly larger than the experimental uncertainties. The uncertainties in species yield and $\frac{\Delta H_c^{eff}}{\Delta H_c^{comp}}$ which were calculated using Equation 46 and illustrated as the shaded regions in Figure 21, are summarized in Table 17. In the figure, the error bars represent experimental uncertainties expressed as two standard errors.

Table 17. Uncertainties in modeled species yields and $\frac{\Delta H_c^{eff}}{\Delta H_c^{comp}}$ for OSB

| **Modeled quantity** | **Uncertainty** |
|---|---|
| $\mathrm{Yield_{CO}}$ | ± 0.025 |
| $\mathrm{Yield_{PM}}$ | ± 0.004 |
| $\mathrm{Yield_{THC}}$ | ± 0.023 |
| $\mathrm{Yield_{CO2}}$ | ± 0.111 |
| $\frac{\Delta H_c^{eff}}{\Delta H_c^{comp}}$ | ± 0.080 |

There exists a minimum characteristic time below which the $CO_2$-yield model and $\frac{\Delta H_c^{eff}}{\Delta H_c^{comp}}$ model no longer produce physically meaningful predictions (i.e., they return negative $CO_2$ yields or negative heats of combustion). For characteristic times shorter than this threshold, the models are not applicable.

The lower applicability limit, denoted $t_{char,min}$, is defined as the smallest characteristic time for which both $CO_2$-yield and $\frac{\Delta H_c^{eff}}{\Delta H_c^{comp}}$ models still provide positive, physically reasonable values. Because $t_{char,min}$ increases with *GER*, a correlation was developed to relate $t_{char,min}$ to ventilation conditions. This allows the lower applicability limit to be determined for any arbitrary *GER* value using this *GER*–$t_{char,min}$ relationship.

To develop this correlation, the minimum characteristic time yielding valid model predictions was identified for each *GER* and listed in Table 18. Therefore, the $CO_2$ and $\frac{\Delta H_c^{eff}}{\Delta H_c^{comp}}$ model will be valid for characteristic times longer than those listed in Table 18 for each corresponding *GER*.

Table 18. Minimum $t_{char}$ that the model is applicable at different *GER*s.

| ***GER*** | $t_{char,min}$, s |
|---|---|
| 0.05 | 0.06 |
| 0.1 | 0.07 |
| 0.3 | 0.08 |
| 0.5 | 0.11 |
| 0.75 | 0.15 |
| 1.0 | 0.30 |
| 1.25 | 0.55 |
| 1.51 | 0.9 |
| 1.75 | 1.16 |
| 2.00 | 1.26 |

For each *GER*, the minimum characteristic time yielding valid model predictions was identified (Table 18), and these values were used to fit the following correlation:

$$t_{char,min} = 0.0662 + \frac{1.283}{1 + e^{-4.261\,(GER - 1.361)}} \quad 51$$

where $t_{char,min}$ is in seconds. This correlation reproduces the observed limits within ±0.10 s for $GER \leq 2.0$. The resulting expression is used to define the lower bound of model validity for both $CO_2$ yield and $\frac{\Delta H_c^{eff}}{\Delta H_c^{comp}}$ calculations, ensuring that the models give physically meaningful values.

### 4.2.5 Validation of the model

To evaluate the performance of the developed model, its predictions were compared with the results of three constant-*GER* tests conducted at *GER* = 0.98 and a lower heat flux of 75 kW m$^{-2}$. These tests were performed with the cap installed and were not included in the model parameterization, which was based on experiments conducted at 95 kW m$^{-2}$. The comparison is presented in Figure 22. A majority of the results show that the experimental data fall within the model's uncertainty bounds, demonstrating the model's ability to reliably predict OSB combustion behavior under conditions different from those used for its development.

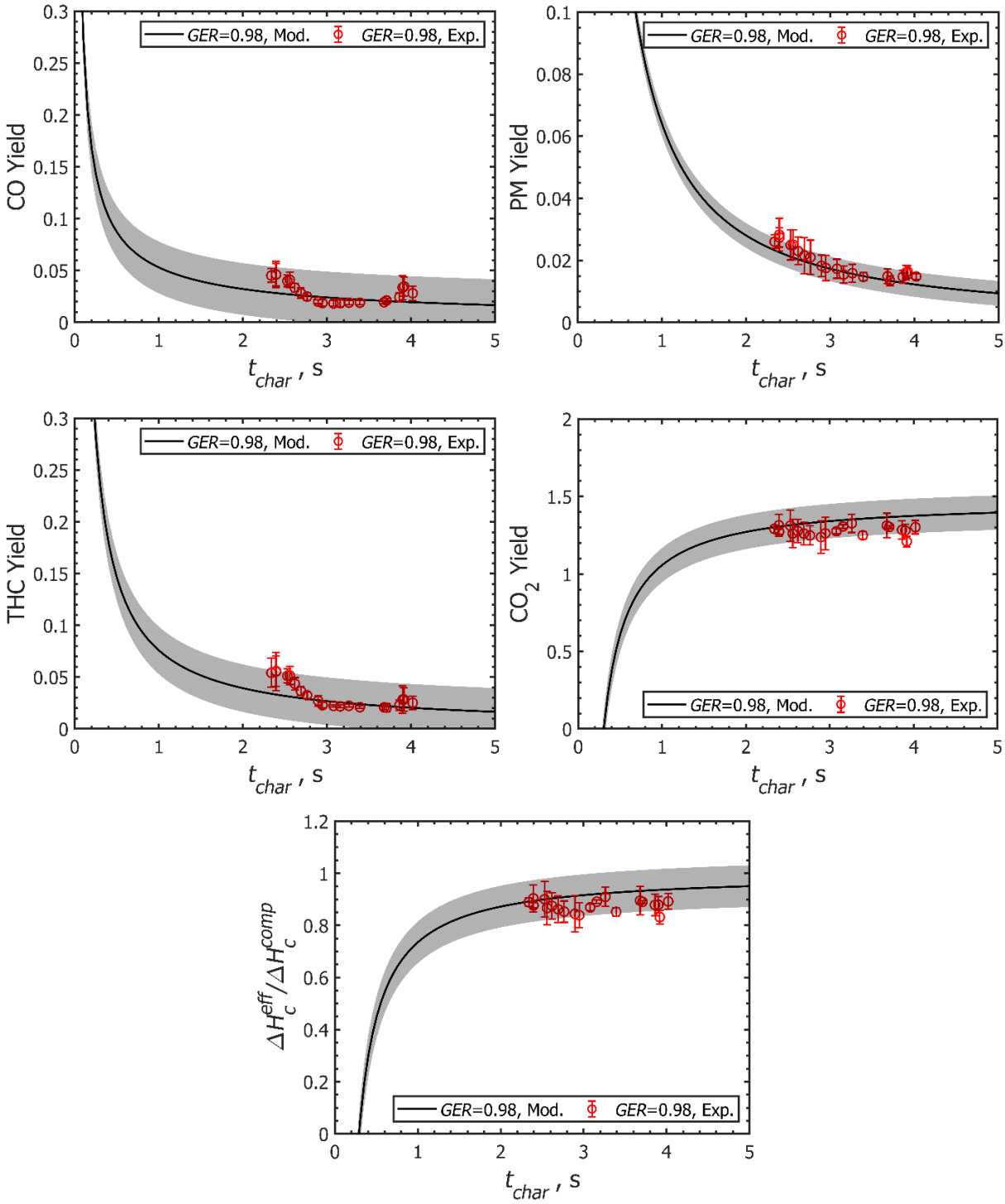


Figure 22. A comparison of experimental and modeled species yields (in mass per mass of OSB pyrolyzate) and $\frac{\Delta H_c^{eff}}{\Delta H_c^{comp}}$

*The experimental data were obtained at 75 kW m$^{-2}$ (GER = 0.98). Shaded areas are model uncertainties computed using Eq. 46.*

### 4.2.6 Comparison of the model prediction with literature data

Tewarson et al. (1993) published FPA measurements of $CO_2$, CO, THC, and PM yields for pine wood across a broad range of *GER* values. Their paper, however, does not include enough detail to calculate the residence time, $t_{char}$. In order to apply the present model, $t_{char}$ was approximated as the average value determined from the OSB experiments at 95 kW $m^{-2}$ in this study for each *GER.* Average $t_{char}$ values at *GER*s of 0.5, 0.98, and 1.5 are 2.02 s, 2.69 s, and 2.98 s, respectively. Figure 23 compares the model predictions with the data of Tewarson et al., with their stated experimental uncertainty (±5%) shown as error bars.

The agreement between the two datasets is generally good for all measured species when comparing the current study with the work of Tewarson et al. The largest discrepancy appears in the THC yields, which leads to an underestimation of the carbon balance (by as much as 10%) when Tewarson's values are used, as illustrated in Figure 23. In their methodology, yields at different ventilation conditions were derived by multiplying species-yield ratios by the corresponding well-ventilated values (Tewarson, Jiang, & Morikawa, 1993). Because the reported well-ventilated THC yield is extremely small relative to CO and PM, even a minor absolute error in this baseline value propagates into a disproportionately large uncertainty in the calculated THC yields. This likely contributes to the substantial differences observed between THC yields reported in the two studies.

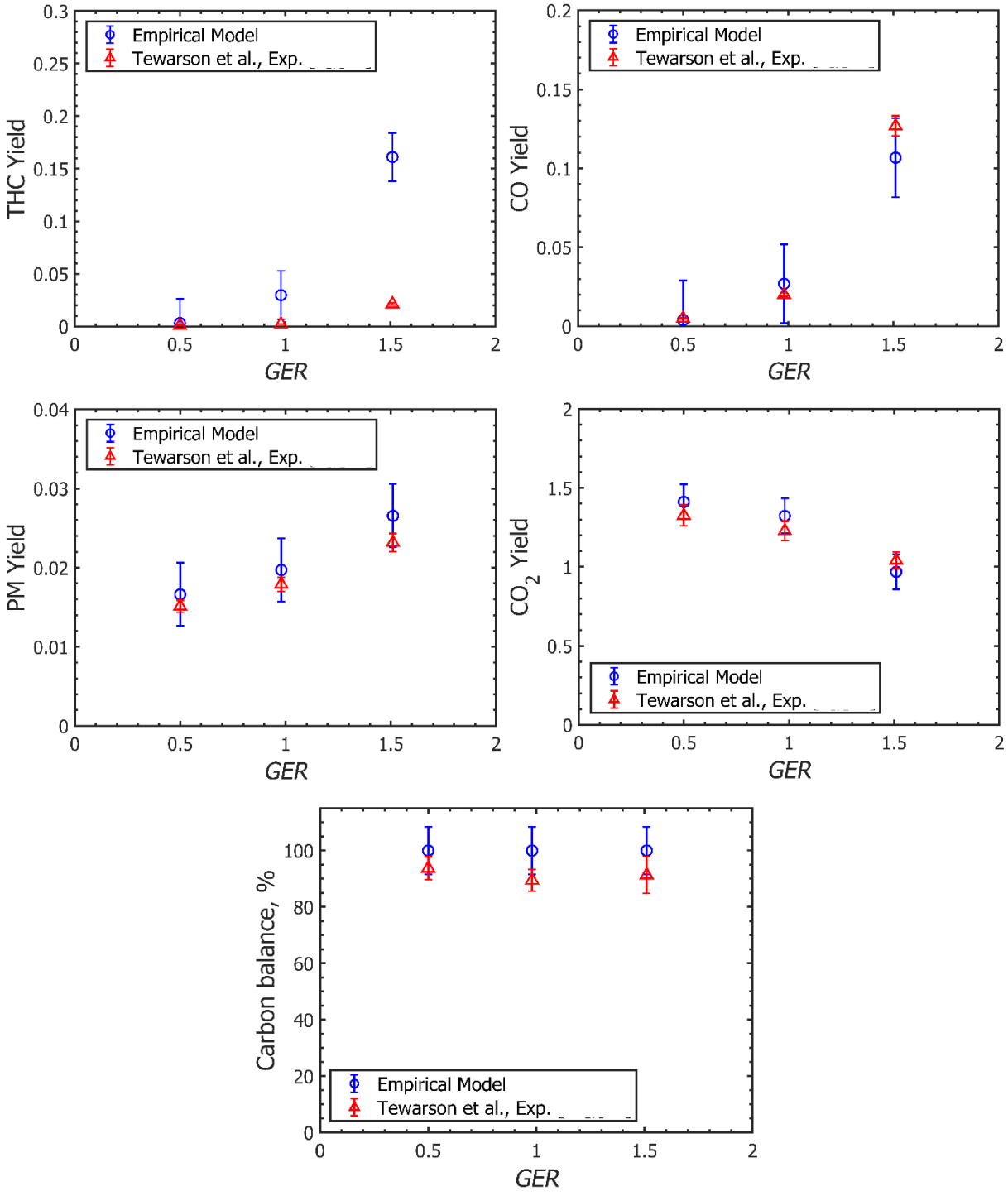


Figure 23. Comparison of species yields and carbon balance measured for pine wood using FPA with current model

*Model prediction obtained at average $t_{char}$ of each GER. The error bars of current data are model uncertainties computed using Eq. 46. The ± 5% uncertainties reported by Tewarson et al. for their experimental data are also shown on the graphs.*

### 4.2.7 Heat release rate per unit area ($HRRPUA^t$)

It is shown here that the model developed for OSB species yields and $\Delta H_c^{eff}$ can also be applied to calculate $HRRPUA^t$. The same method as PMMA, used here for OSB $HRRPUA^t$ calculation. The $\frac{\mu_{O2}}{\mu_{CO2}}$ ratio in Equation 26 was computed from the modeled species yields using Equation 39, which were evaluated for each 10-second interval using the corresponding *GER* and $t_{char}$.

$HRRPUA^t$ was calculated for all FPA experiments conducted at 95 kW m$^{-2}$, including both constant- and variable-*GER* segments of the tests. The results are shown in Figure 24. The uncertainties plotted in the figure as shaded area reflect the model uncertainty, assumed to be equal to that of the $\frac{\Delta H_c^{eff}}{\Delta H_c^{comp}}$ values reported in Table 17. As expected, the results demonstrate that increasing *GER* leads to a decrease in $HRRPUA^t$.

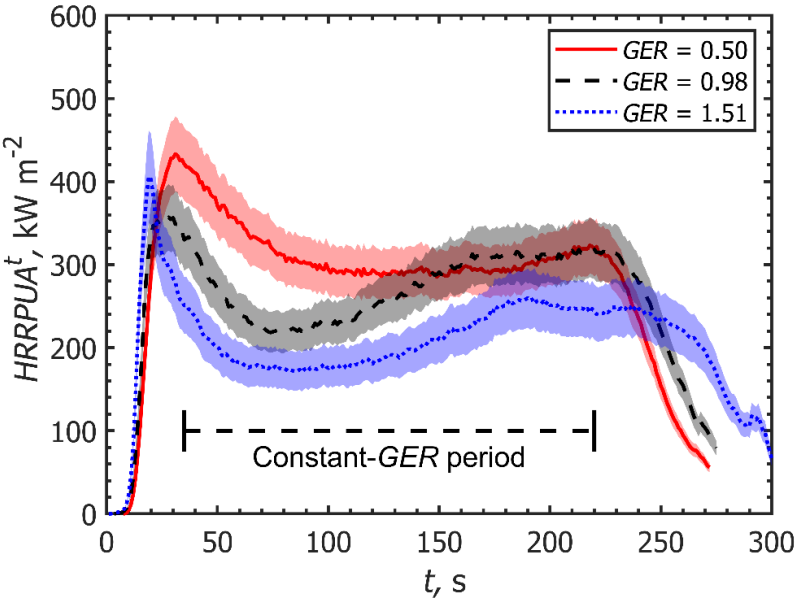


Figure 24. OSB heat release rates per unit area computed for OSB experiments performed at 95 kW m$^{-2}$ heat flux.

# 5 Conclusions

In this study, a novel methodology was developed to maintain constant Global Equivalence Ratio, *GER,* during combustion experiments using a modified Fire Propagation Apparatus (FPA). Constant ventilation condition was achieved through precise control of the air flow rate into the test section, allowing *GER* to remain fixed despite continuous changes in the pyrolyzate generation rate. A wide range of constant-*GER* values (0.50 to 1.96), spanning both over- and under-ventilated conditions, was successfully implemented. This approach overcomes a major

limitation of previous studies, in which time-varying *GER* introduced substantial uncertainty in relating product yields to ventilation conditions. Detailed measurements of $CO_2$, CO, THC, NO, HCN, and PM were obtained using calibrated analyzers, and the characteristic residence time of the combusting mixture in the test section was incorporated directly into the analysis and modeling.

The PMMA results show that both *GER* and $t_{char}$ influence species yields and effective heat of combustion, $\Delta H_c^{eff}$. As *GER* increased from 0.63 to 1.96, the $CO_2$ yield dropped from 2.04 to 1.05 (mass per mass of pyrolyzate), while $\Delta H_c^{eff}$ decreased from 23.6 kJ $g^{-1}$ to 15.1 kJ $g^{-1}$ indicating reduced combustion efficiency. Meanwhile, the yields of CO, PM, and THC increased from 0.019 to 0.263, from 0.015 to 0.051, and from 0.006 to 0.301, respectively, over the range of studied *GERs*. NO and HCN yields also showed increasing trends with *GER* as well, although measured values were close to the detection limits of the corresponding sensors, leading to large uncertainties in these quantities. Carbon balance remained within ±5% for all conditions, supporting the reliability of the measurements.

A novel method was developed for deriving the heat of combustion based on the stoichiometric coefficients calculated from the species yield and heat of combustion per unit mass of consumed $O_2$ (13.1 kJ $g_{O2}^{-1}$), while using the mass generation flow rate of $CO_2$ in the calculation. This approach enables a more accurate estimation of $\Delta H_p$ in FPA experiments (where $O_2$ measurements are less reliable than $CO_2$ measurements due to high dilution) while avoiding the use of fuel-specific constants in the calculation. $HRRPUA^t$ results for each constant-*GER* condition were calculated using this method. Using these measurements, an empirical model was developed to predict species yields and $\Delta H_c^{eff}$ as functions of *GER* and $t_{char}$, and model predictions showed good agreement with validation tests performed under different *GER* and heat-flux conditions.

This methodology was then extended to a charring material—oriented strand board (OSB)—to evaluate its applicability under more complex decomposition and combustion behavior. Constant-*GER* conditions (0.50, 0.98, and 1.51) were successfully achieved for OSB. As *GER* increased from 0.50 to 1.51, the $CO_2$ yield decreased from 1.394 to 1.026 (mass per mass of pyrolyzate), and the effective heat of combustion, $\Delta H_c^{eff}$, decreased from 14.20 to 10.83 kJ $g^{-1}$, indicating reduced combustion efficiency. Correspondingly, the yields of CO, PM, and THC increased from 0.0044 to 0.1207, from 0.0169 to 0.0279, and from 0.0035 to 0.1809, respectively. The resulting species yields showed strong dependence on both *GER* and $t_{\text{char}}$, similar to PMMA, but with additional variability caused by the evolving pyrolyzate composition. Analysis of the pyrolyzate-composition effects showed that these changes have a measurable but

secondary influence on species production compared with the dominant roles of *GER* and $t_{char}$. A multi-component pyrolyzate and unburned THC compositions were characterized through dedicated pyrolysis experiments. These findings highlight the added complexity of characterizing charring fuels combustion behavior and their modeling. An empirical model was developed to predict species yields and the effective heat of combustion under different combinations of *GER* and $t_{\text{char}}$.

# 6 References


ASTM International. (2016). *ASTM D5373–16: Standard test methods for instrumental determination of carbon, hydrogen, and nitrogen in laboratory samples of coal and coke.* West Conshohocken, PA, USA.

ASTM International. (2019). *ASTM E2058–19: Standard test methods for measurement of material flammability using a Fire Propagation Apparatus (FPA).* doi:https://doi.org/10.1520/E2058-19

Beyler, C., Croce, P., Dubay, C., Johnson, P., & McNamee, M. (2017). Oxygen consumption calorimetry, William Parker: 2016 DiNenno Prize. *Fire Science Reviews, 6*(1). doi:https://doi.org/10.1186/s40038-016-0016-z

Biteau, H., Steinhaus, T., Simeoni, A., Schemel, C., Marlair, G., Bal, N., & Torero, J. (2008). Calculation Methods for the Heat Release Rate of Materials of Unknown Composition. *Fire Safety Science, 9*, 1165-1176.

Chaffer, R. (2021). A redesign of the fire propagation apparatus to simplify manufacturing and increase measuring capabilities, M.S. thesis. University of Maryland, College Park, MD, USA.

Chen, D., Liu, X., Han, J., Jiang, M., Xu, Y., & Xu, M. (2018). Measurements of particulate matter concentration by the light scattering method: Optimization of the detection angle. *Fuel Processing Technology, 179*, 124–134. doi:https://doi.org/10.1016/j.fuproc.2018.06.016

FAA. (2020). *Heat Release Rate Test for Cabin Materials, FAA Aircraft Materials Fire Test Handbook.* Retrieved from https://www.fire.tc.faa.gov/pdf/handbook/00-12_ch5-0909.pdf

Gerhart, A., Hochstein, J., & Gerhart, P. (2020). *Munson, Young and Okiishi's Fundamentals of Fluid Mechanics (9th ed.).* Wiley, Hoboken, NJ, USA.

Han, J., Liu, X., Jiang, M., Wang, Z., & Xu, M. (2021). An improved on-line measurement method of particulate matter concentration using tri-wavelength laser light scattering. *Fuel, 302*. doi:https://doi.org/10.1016/j.fuel.2021.121197

Hinshaw, J. (2005). The flame ionization detector. *LCGC Chromatography Online, 23*(12), 1262-1272. Retrieved from https://www.chromatographyonline.com/view/flame-ionization-detector

Hu, F., Li, P., Guo, J., Wang, F., Wang, K., Jiang, X., . . . Zheng, C. (2018). Optimal Equivalence Ratio to Minimize NO Emission during Moderate or Intense Low-Oxygen Dilution Combustion. *Energy and Fuels, 32*(4), 4478–4492. doi:https://doi.org/10.1021/acs.energyfuels.7b03162

Hull, T., Carman, J., & Purser, D. (2000). Prediction of CO evolution from small-scale polymer fires. *Polymer International, 49*(10), 1259–1265.

Hurley, M., Gottuk, D., Hall, J., Harada, K., Kuligowski, E., Puchovsky, M., . . . Wieczorek, C. (2016). *SFPE Handbook of Fire Protection Engineering.* Springer New York. doi:https://doi.org/10.1007/978-1-4939-2565-0

ISO-TS-19700. (2007). Controlled equivalence ratio method for the determination of hazardous components of fire effluents. ISBN 978 0 580 93304 2 (ISO/TS 19700:2016).

P. B. Keady. (2000). "Application Note ITI-075". *vol. 2*. TSI Incorporated Shoreview, Minnesota.

Pitts, W. (1995). The global equivalence ratio concept and the formation mechanisms of carbon monoxide in enclosure fires. *Progress in Energy and Combustion Science, 21*(3), 197–237.

Roy, S. (2022). *A redesign of the exhaust and gas sampling system of the fire propagation apparatus* . (Master's thesis). University of Maryland, College Park, MD, USA.

Shafizadeh, F. (1982). Introduction to pyrolysis of biomass. *Journal of Analytical and Applied Pyrolysis, 3*(4), 283–305. doi:https://doi.org/10.1016/0165-2370(82)80017-X

Tewarson, A., Jiang, F., & Morikawa, T. (1993). Ventilation-controlled combustion of polymers. *Combustion and Flame, 95*(1-2), 151–169.

Tian, B., Gao, Y., Balusamy, S., & Hochgreb, S. (2015). High spatial resolution laser cavity extinction and laser-induced incandescence in low-soot-producing flames. *Applied Physics B, 120*, 469–487. doi:10.1007/s00340-015-6156-3